Analysis of the SAR Imaging Process of the Ocean Surface Using Volterra Models

Jean-Marc Le Caillec, René Garello, *Senior Member, IEEE*, and Bertrand Chapron

Abstract—**In this paper, the synthetic aperture radar (SAR) process of the ocean surface mapping is studied using a decomposition based on a Volterra model. By a mathematical expansion of the complex exponential of the complete SAR transform, these models decompose the nonlinear distortion mechanisms of the SAR spectrum over different spectra of polynomial interactions. Thus, they offer an alternative modeling (to the exact SAR transform) giving a theoretical separation between the SAR Fourier components linearly derived from the sea surface elevation and the artifacts created by nonlinearities of the SAR mapping of the ocean surface. The main results of this paper consist of the systematic assessment of such an approximation of the ocean surface SAR imaging process. Higher order statistics (HOS) of the SAR transform and their calculus and implementation are presented. In fact, nonlinearity detection, location (in the Fourier domain) and quantification can only be performed by HOS, reduced here to a second-order Volterra Model. The Volterra expansion of the SAR imaging process opens new theoretical inversion schemes since under certain conditions on the linear part, Volterra models are easily invertible. Our method is first tested on simulated SAR images in order to validate the HOS tools. We then show results of this nonlinearity analysis performed on images from the ERS-1 satellite and we present cases of nonlinearity detection.**

Index Terms—**Higher order statistics, radar mapping, SAR, sea surface, Volterra models.**

I. Introduction

A SYNTHETIC aperture radar (SAR) is an active electromagnetic instrument which allows the detection of large scenes with very high resolution. It is independent of the diurnal cycle and weather conditions. Fig. 1 presents a sea surface imagette obtained by the ERS-1 SAR. Visible crest lines of this radar image are about five kilometers long. Such waves are not too common and this image can be considered as an illustrative example of the known distortion associated with SAR mapping [9]. From the pioneering work of Alpers and Rufenach [1] and [4], the SAR imaging process of the sea surface has been widely studied and is indeed known to be nonlinear (i.e., it does not satisfy the classical criteria of linear systems [26]).

Current SAR transform decomposition of the sea mapping is usually achieved in two steps. The first one consists of the modulation of the backscattered energy (around its mean σ_0) by the sea surface. This step is divided into two different mechanisms: a geometric effect known as the tilt modulation, due to the variation of the angle between the sea surface and the radar beam (see [28], [29]) and a hydrodynamic effect due to the non uniformity of the gravity capillary wave spectrum. The backscattered energy is proportional to this spectrum for Bragg backscattering [2], [11], [16], [22]. Although many parameters are still unknown, this latter hydrodynamic modulation is assumed to be linear. Both modulations produce a real aperture radar (RAR) image, i.e., an image of the frozen sea surface. The second step in SAR mapping is the modulation associated with the sea surface motion. Orbital wave velocities produce Doppler shifts leading to $d(x)$ misplacements of the RAR pixel in the SAR image (so-called "velocity bunching").

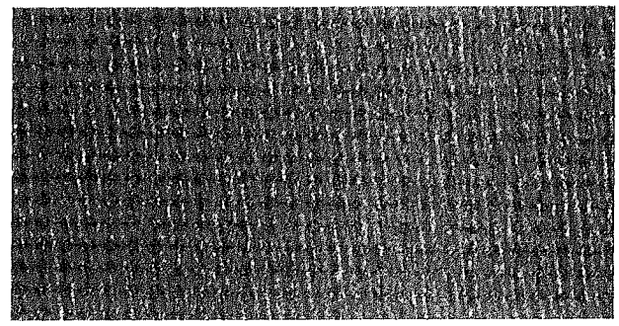

Fig. 1. SAR image of the sea surface.

Following Hasselmann and Hasselmann [9], SAR Fourier coefficients are given by

$$\tilde{X}_{\mathrm{sar}}(k) = |A|^{-1} \cdot \int_A X_{\mathrm{rar}}(x) \cdot e^{j \cdot k \cdot d(x)} \cdot e^{-j \cdot k \cdot x} \cdot dx \quad (1)$$

where A is a given surface and x a two-dimensional (2-D) array having a range and azimuthal components. For the remaining part of this paper, k_x will denote the azimuthal component of the wavenumber vector k while k_y will be the range component. Since the displacement is along the azimuthal axis we then have $k \cdot d(x) = k_x \cdot |d(x)|$. The complete nonlinear transform presented in (1) includes the decrease in effective resolution caused by the stretching/contraction of the RAR pixel due to the orbital velocity dispersion into the radar resolution cell. Following such a model, the SAR mapping nonlinearity comes from the complex exponential in expression (1).

The first main contribution of this paper is to expose and examine the approximation of the complete nonlinear transform by a Volterra model. We list below four reasons why such an approximation is of interest.

- First, this decomposition will help to better understand the nonlinear SAR transform. In Volterra models, the nonlinear interactions are explicitly separated into nonlinear interactions of different orders and consequently the nonlinear interactions are separated in the frequency domain

Manuscript received April 18, 2000; revised April 9, 2002.

J.-M. Le Caillec and R. Garello are with the ENST de Bretagne, Dpt ITI, Technopôle Brest-Iroise, Brest-Cedex BP 832, 29285, France.

B. Chapron is with the IFREMER, DRO/OS, Plouzané BP 70, 29280, France.

Publisher Item Identifier S 0364-9059(02)06304-5.

as will be seen in Section IV-A. The identification of different orders of nonlinear interactions (especially the linear and quadratic components) facilitate the comprehension of the nonlinearity analysis (i.e., detection, location and quantification of nonlinearity) using higher order statistics (HOS) as detailed in Section II and enables the amount of nonlinear energy "created" by the nonlinear SAR transform to be quantified, and a decision to be made concerning whether the process is linear or not.

- Although the SAR spectrum expansion has been already investigated by Krogstad [15] in the one-dimensional (1-D) case, the 2-D case can present spectrum rotation (not conveyed in the 1-D case). One of the contributions of this paper is to better understand such phenomena by expanding the SAR spectrum over polynomial spectra as stated above.
- Nonlinear time-series modeling using HOS methods with an underlying Volterra modeling makes it possible to estimate unknown Volterra kernels. Applied to the SAR process, these methods would allow the RAR transfer function to be identified and then the usual assumption of linearity at this stage of the SAR imaging process to be verified. These methods can work whether input data of the Volterra model, i.e., measured sea elevation, (see for instance [13], [20], [25]) are available or not ([17]).
- Finally, the Volterra decomposition makes it possible to easily invert the SAR transform. Indeed, Volterra models, under some restrictions on the first kernel, are post-invertible by another Volterra model. This means that the kernels of this post-inverse model are derived from those of the direct Volterra model. Moreover, this new inversion scheme can be performed directly on the image and not only on the spectrum like the regularized inversion process proposed by Hasselmann and Hasselmann in [9]. Single look complex (SLC) images being widely used nowadays, there is great interest in finding an inversion process conserving the phase information (i.e., complex data). However, before inverting the SAR transform, a systematic verification of the validity of the SAR transform expansion using Volterra kernels must be performed. The main part of this paper is devoted to this subject.

Another important contribution of this paper lies in the theoretical calculation of the SAR transform bispectrum. We recall that nonlinearity analysis from an observed output of possibly nonlinear systems without input data (that is generally the case with SAR image) can only be performed with HOS. Obviously, both contributions are closely linked since, as will be seen in Section II-B, the SAR transform bispectrum is not easy to interpret. Volterra models are useful in this case since existing methods of nonlinear systems identification by HOS usually assume a Volterra modeling. For instance, the methods for nonlinearity location and quantification use HOS but also assume that the nonlinear system is a second-order Volterra model.

When dealing with SAR nonlinearity analysis with Volterra models and HOS, our first step involves recalling the basic results of the different domains tackled in this paper. HOS theory is discussed in the first section, while classical and new results concerning the SAR transform spectrum and bispectrum are given in the second section. Section III is devoted to Volterra models and to the SAR transform expansion using these models from a theoretical point of view. In Section IV-A, we develop a comparison between the SAR spectrum obtained by the complete nonlinear transform of (1) and the spectrum of Volterra models of different orders in order to examine the validity of the SAR transform expansion using Volterra models. For this comparison, we compute the spectra by assuming the sea surface to be Gaussian distributed and derived from a JONSWAP spectrum [12]. Some of the sea states that we will examine are not realistic especially the combination of certain wavelengths and significant wave heights H_s (defined as $H_s = 4\sqrt{E\{\zeta^2(x)\}}$ where $\zeta(x)$ is the sea surface elevation). Nevertheless, since our purpose is to examine the SAR transform decomposition on Volterra models, feasibility must be verified for all sea states within a reasonable sea parameter range (H_S between 0 and 10 m and wavelength between 100 and 500 m). Nonlinearity analysis being necessarily performed with HOS, the validity of the SAR decomposition for third-order statistics is presented in Section IV-B. This validity is verified from the point of view of bispectrum distances and from the point of view of nonlinearity statistical index values (used for nonlinearity detection) in the hypothesis testing framework. Section V presents nonlinearity analysis for real SAR images (from the ERS-1 satellite) in light of the results presented in the previous sections. We show that we can detect nonlinear events when they are present in the images.

II. Nonlinearity Analysis and Higher Order Spectra

When dealing with nonlinearity issues, we must first address the problem of the presence or the absence of nonlinearity in the observed signal. If nonlinearities are present, we then have to identify which Fourier component artifacts it has produced. A second step of the analysis thus consists of a nonlinearity location in the Fourier domain and we finally have to perform the estimation of the Fourier component energy part provided by this nonlinearity, i.e., the quantification of the nonlinearity. This nonlinearity analysis can only be performed with higher order spectra.

A. Definitions and Properties

In the Fourier domain, the information concerning the signal is divided into the magnitude and phase of the Fourier coefficients. The spectrum can be defined as the Fourier transform of the autocorrelation function or as the mathematical expectation of the Fourier transform coefficients

$$\begin{aligned} S(k) &= \sum_{n=-\infty}^{+\infty} M_2^X(n) e^{-j\cdot k\cdot n} = E\left\{\tilde{X}(k)\cdot\tilde{X}^*(k)\right\} \\ \text{with } M_2^X(n) &= E\{X(i)\cdot X(i+n)\} \\ \text{and } \tilde{X}(k) &= \sum_{n=-\infty}^{+\infty} X(n) e^{-j\cdot k\cdot n}. \end{aligned} \tag{2}$$

A spectrum, being real valued, does not provide phase information but, polyspectra and especially bispectra can convey phase information (these quantities being complex valued). The third-

order moment of a stationary signal is expressed as the mathematical expectation of the triple product of the discrete signal

$$M_3^X(n_1,n_2) = E\{X(i)\cdot X(i+n_1)\cdot X(i+n_2)\}. \quad (3)$$

The third-order cumulant is then defined by

$$C_3^X(n_1,n_2) = M_3^X(n_1,n_2) - I_0\cdot M_2^X(n_1-n_2) - I_0\cdot M_2^X(n_1) - I_0\cdot M_2^X(n_2) + 2I_0^3 \quad (4)$$

where I_0 is the mean of the process.

For zero mean processes, the third-order cumulant and moment are then equal. A fundamental property of the third-order cumulant is that it is null for Gaussian processes [19], [21]. The bispectrum can be defined as the Fourier transform of the third-order cumulant or as the mathematical expectation of the Fourier transform of the signal

$$\begin{aligned} B(k_1,k_2) &= \sum_{n_1=-\infty}^{+\infty}\sum_{n_2=-\infty}^{+\infty} C_3^X(n_1,n_2)\, e^{-j(k_1\cdot n_1+k_2\cdot n_2)} \\ &= E\left\{\tilde{X}(k_1)\cdot\tilde{X}(k_2)\cdot\tilde{X}^*(k_1+k_2)\right\} \\ &\quad - I_0\cdot S(k_1)\,\delta(k_1+k_2) - I_0\cdot S(k_1)\,\delta(k_2) \\ &\quad - I_0\cdot S(k_2)\,\delta(k_1) + 2I_0^3\delta(k_1)\,\delta(k_2) \end{aligned} \quad (5)$$

Mechanisms for nonlinearity detection using phase coupling detection (i.e., phase coherence detection) are explained in Appendix A and are detailed again on a second-order Volterra model in Section III-A.

When studying nonlinearities, bicoherence is a fundamental quantity which can be derived from higher order spectra. It can be seen as the normalized bispectrum, and is defined by

$$P(k_1,k_2) = \frac{|B(k_1,k_2)|^2}{S(k_1)\cdot S(k_2)\cdot S(k_1+k_2)}. \quad (6)$$

In the case of a linear process, the bicoherence becomes flat, i.e., constant for all pairs (k_1, k_2) [8]. The nonlinearity index, proposed by Subba Rao and Gabr in [27] and recalled in Appendix A, tests whether the estimated bicoherence samples have the same mean (flatness test). This is a statistical hypothesis testing providing only a probability α, generally equal to 0.9 or 0.95 (and called the "significance level"), that the signal is linear. The usual procedure for hypothesis testing is to set up this probability and to theoretically derive a reference threshold of the statistical index from its theoretical pdf, under the hypothesis that the signal is linear. If the measured index is lower than this threshold, the image is declared to be linear with a probability α while if it is greater, the observed image is declared to be nonlinear. Two important parameters for statistical hypothesis testing are as follows.

- "Type I Error" probability: That is the probability of declaring an image to be nonlinear although it is linear. The probability is then given by $(1-\alpha)$.
- "Type II Error" probability: That is the probability of classifying an image as linear although nonlinear. The probability is denoted β.

For a fixed value of α, the smaller β is, the easier the detection of nonlinearity will be, since errors of misclassification are reduced. The β parameter depends on the theoretical spectrum and bispectrum of data contrary to α, which depends only on the faet that the bicoherence is flat.

B. Spectrum and Bispectrum of the Complete SAR Transform

From (1), the SAR spectrum can easily be calculated using a Gaussian assumption for the sea surface [9], [14]

$$\begin{aligned} S_{\text{sar}}(k) &= E\left\{\left|\tilde{X}_{\text{sar}}(k)\right|^2\right\} \\ &= \sigma_0^2\left[e^{-(k_x)^2\cdot M_2^{dd}(0)}\right. \\ &\quad \left.\cdot\int_{-\infty}^{+\infty} e^{(k_x)^2\cdot M_2^{dd}(x)} C(x,k_x)\cdot e^{-j\cdot k\cdot x}dx - \delta(k)\right] \end{aligned} \quad (7)$$

with

$$\begin{aligned} G(x,k_x) = &\left(1+M_2^{rr}(x)+j\cdot k_x\cdot\left(M_2^{rd}(x)-M_2^{rd}(-x)\right)\right. \\ &\left.+k_x^2\cdot\left(M_2^{rd}(0)-M_2^{rd}(x)\right)\cdot\left(M_2^{rd}(0)-M_2^{rd}(-x)\right)\right) \end{aligned}$$

where $M^{rr}(x) = E\{X_{\text{rar}}(0)X_{\text{rar}}(x)\}$ is the RAR image autocorrelation, $M^{rd}(x) = E\{X_{\text{rar}}(0)X_d(x)\}$ is the cross correlation between the RAR image and the displacement due to velocity bunching and $M^{dd}(x) = E\{X_d(0)X_d(x)\}$ is the displacement autocorrelation. The coefficient $e^{-k_x^2\cdot M_2^{dd}(0)}$ conveys the loss of resolution due to azimuth smearing. Assuming that the RAR function is linear, the bispectrum is given by (8) shown at the bottom of the page, with

$$\begin{aligned} A(k_x^1,k_x^2,x,x') = &1 + j\left(k_x^1\left(M^{rd}(x'-x) - M^{rd}(x')\right)\right. \\ &\left.+ k_x^2\left(M^{rd}(0) - M^{rd}(x')\right)\right) \\ B(k_x^1,k_x^2,x,x') = &1 + j\left(k_x^1\left(M^{rd}(0) - M^{rd}(x)\right)\right. \\ &\left.+ k_x^2\left(M^{rd}(x-x') - M^{rd}(x)\right)\right) \end{aligned}$$

$$\begin{aligned} B_{\text{sar}}(k_1,k_2) = &\sigma_o^3\cdot e^{-((k_x^1)^2+(k_x^2)^2+k_x^1\cdot k_x^2)\cdot M_2^{dd}(0)} \\ &\cdot\int_{-\infty}^{+\infty}\int_{-\infty}^{+\infty} e^{\left(-M_2^{dd}(x_1-x_2)\cdot k_x^1\cdot k_x^2 - M_2^{dd}(x_1)\cdot(k_x^1-k_x^2)\cdot k_1 + M_2^{dd}(x_2)\cdot(k_x^1+k_x^2)\cdot k_2\right)} \\ &\left[M^{rr}(x)\cdot A(k_x^1,k_x^2,x,x') + M^{rr}(x')\,B(k_x^1,k_x^2,x,x') + M^{rr}(x-x')\,C(k_x^1,k_x^2,x,x')\right. \\ &\left.+ j\cdot A(k_x^1,k_x^2,x,x')\cdot B(k_x^1,k_x^2,x,x')\cdot C(k_x^1,k_x^2,x,x')\right]\cdot e^{-j\cdot(k_1\cdot x_1+k_2\cdot x_2)}dx_1\cdot dx_2 \\ &- \sigma_o S(k_2)\cdot\delta(k_1) - \sigma_o S(k_1)\cdot\delta(k_2) - \sigma_o S(k_1)\,\delta(k_1+k_2) - \sigma_o^3\cdot\delta(k_1)\,\delta(k_2) \end{aligned} \quad (8)$$

$$C\left(k_x^1, k_x^2, x, x'\right) = 1 + j\Big(k_x^1\left(M^{rd}(-x) - M^{rd}(0)\right) + k_x^2\left(M^{rd}(-x') - M^{rd}(0)\right)\Big) \quad (9)$$

and k_x^1, k_x^2 are the azimuthal component of the wavenumber vectors k_1, k_2, respectively. This result is achieved by introducing (1) into the second definition of the bispectrum definition (see (5)) and proceeding like Krogstad [14] (see Appendix B). Extracting information from the complete transform bispectrum is not easy, because of the complexity of the expression. Indeed, higher order moments are expressed as a product of the second-order moments of Gaussian fields, i.e., the displacement of the RAR pixel and the RAR pixel itself which are both linearly linked to the sea surface. Furthermore, because the bispectrum support is a four-dimensional (4-D) structure, a simple analysis is not possible. However for the quasi-linear transform [9], obtained by expanding the exponential in (8) (k_x^1 and k_x^2 small), bispectrum is found to be null, since the SAR image is thus a linear filtering of a Gaussian sea surface.

III. Volterra Model's

A. Definition and Properties

Volterra models are commonly used for nonlinearity analysis and have been developed by Schetzen [26]. In these models, the output values $Y(n)$ can be expressed as a polynomial of input data

$$Y(n) = h_0 + \sum_{i=1}^{N} f_i\left(X(n)\right) \quad (10)$$

with

$$f_i\left(X(n)\right) = \sum_{n_1=-\infty}^{+\infty} \cdots \sum_{n_i=-\infty}^{+\infty} h_i\left(n_1, \ldots, n_i\right) \cdot X\left(n - n_1\right) \cdots X\left(n - n_i\right) \quad (11)$$

or in the Fourier domain

$$\tilde{Y}(k) = h_0\delta(k) + H_1(k)\tilde{X}(k) + \sum_{i=2}^{N} TF\left(f_i\left(X(n)\right)\right) \quad (12)$$

with

$$TF\left(f_i\left(X(n)\right)\right) = \int_{-\infty}^{+\infty} \cdots \int_{-\infty}^{+\infty} H_i\left(k - \sum_{l=1}^{i-1} k_l, k_1, \ldots, k_{i-1}\right) \tilde{X}\left(k - \sum_{l=1}^{i-1} k_l\right) \cdot \tilde{X}\left(k_1\right) \cdots \cdot \tilde{X}\left(k_{i-1}\right) dk_1 \cdots dk_{i-1} \quad (13)$$

and $i \geq 2$. The term $h_i(n_1, \ldots, n_i)$ is the i th-order kernel of the Volterra series (which generalizes the Taylor development) and $H_i(k - \sum_{l=1}^{i-1} k_l, k_1, \ldots, k_{i-1})$ its Fourier transform. We can interpret Volterra models as a bank of filters, extending the linear case [seen as a first-order Volterra model (FOVM)]. The main idea behind Volterra models is to relate the usual transfer function concept to more general cases involving nonlinearities and to describe simply the frequency behavior of this nonlinear transfer function. For instance, an analytic expression of the second-order Volterra model (SOVM) in the Fourier domain is given by (setting $N = 2$ in (10))

$$\tilde{Y}(k) = H_1(k)\tilde{X}(k) + \int_{-\infty}^{+\infty} H_2\left(k_j, k - k_j\right)\tilde{X}\left(k_j\right) \cdot \tilde{X}\left(k - k_j\right) dk_j. \quad (14)$$

The output of the quadratic kernel is the interaction between two harmonics of the input signal weighted by $H_2(k_j, k - k_j)$, the wavenumber sum of these two waves being equal to k. The spectrum $S_{\mathrm{N}}(k)$ of the Volterra model of order N can be written by introducing (10) in (2) as

$$S_{\mathrm{N}}(k) = \sum_{p=1}^{N}\sum_{q=1}^{p} S_{p,q}(k) \quad (15)$$

where $S_{p,q}(k)$ is the cross spectrum between the interactions of orders p and q as seen in Appendix C. Under the Gaussian input data assumption, $S_{p,q}(k)$ is non null only if $p + q$ is even (see also Appendix C). For instance, the SOVM spectrum is given by

$$S_2(k) = S_{1,1}(k) + S_{2,2}(k) = |H_1(k)|^2 E\left\{\left|\tilde{X}(k)\right|^2\right\} + \int_{-\infty}^{+\infty} |H_2\left(k_j, k - k_j\right)|^2 \cdot E\left\{\left|\tilde{X}\left(k_j\right)\tilde{X}\left(k - k_j\right)\right|^2\right\} dk_j. \quad (16)$$

The SOVM spectrum is thus the sum of a linear "spectrum" and a "quadratic" spectrum. As discussed in [18], the quadratic interactions of a real finite bandwidth signal, such as the sea surface, are divided into two spectra.

- One is located over the low wavenumber components (called destructive interactions, because they are produced by two waves with opposite wavenumbers).
- The other, the constructive interaction spectrum, is centered on twice the dominant wavelength of the original spectrum.

The third-order Volterra model (TOVM) spectrum, the TOVM model being deduced from the SOVM by adding a cubic kernel, is also the sum of linear, quadratic and cubic spectra, and a supplementary cross linear-cubic spectrum.

In the same manner, the bispectrum of a Volterra model of order N can be calculated by introducing (14) into (5) and is given by

$$B_{\mathrm{N}}\left(k_1, k_2\right) = \sum_{p=1}^{N}\sum_{q=1}^{p}\sum_{r=1}^{q} B_{p,q,r}\left(k_1, k_2\right) \quad (17)$$

in which $B_{p,q,r}(k_1, k_2)$ is the bispectrum of interactions of orders p, q, r. As for the spectrum, the bispectrum is non null only if $p + q + r$ is even (see Appendix C). For instance, the SOVM bispectrum is given by (18) shown at the bottom of the next page. We verify that two kinds of phase coupling are detected by the bispectrum.

- Primary phase-coupling phenomena (PPCP, $B_{2,1,1}\left(k_1, k_2\right)$) occurring between two waves and their quadratic interactions.

- Secondary phase-coupling phenomena (SPCP, $B_{2,2,2}(k_1, k_2)$) existing between three waves created by quadratic interactions.

The advantage of phase–coupling phenomena duality is that nonlinearity detection is still possible even if the linear kernel is identically null, i.e., if all original signal waves have been removed. This case occurs in the SAR transform since for some cases the linear contribution is approximately null. The drawback lies in the difficulty in identifying what kind of phase coupling is detected by the bispectrum, i.e., if the detected phase coupling can be interpreted or not as the phase coupling of two original signal waves and their quadratic interaction. The identification of the kind of phase coupling is important for distinguishing the linear components (i.e., linear spectrum) from the quadratic artifacts possibly observed in a 2-D signal. The use of homogeneous bicoherence tables (HBTs) see Appendix A or [18]) is relevant for determining the kind of phase coupling detected, the PPCP and the SPCP not being located at the same place in these tables. As a matter of fact, in these two tables, the linear signal components cross the lines $k_x^1 = k_x^2$ and $k_y^1 = k_y^2$ and thus the linear spectrum can be located by using this property as will be seen in Sections IV-B and V. However, this method assumes implicitly that the nonlinear system is an SOVM, and for this reason we need to decompose the SAR transform into Volterra models. Finally, the quantification is done by also assuming an SOVM with some restrictions and by estimating the quadratic spectrum by [see (16)]

$$S_{2,2}(k) = S_2(k).T_{RA}(k) \tag{19}$$

where $T_{RA}(k)$ is the cross bicoherence table (CBT) as proved in Appendix A.

B. Application to the SAR Transform

The SAR transform expressed in (1) can always be expanded over Volterra models since the exponential expansion is valid over the complex plane. The discrete space formula of (1) can be written as

$$\begin{aligned}\tilde{X}_{\mathrm{sar}}(k) =& \sum_i X_{\mathrm{rar}}(i) \cdot e^{j \cdot k_x \cdot d(i)} \cdot e^{-j \cdot k \cdot i} \\ \text{with } X_{\mathrm{rar}}(i) =& \sigma_0 \left[1 + \int_{-\infty}^{+\infty} T^{\mathrm{rar}}(k) \tilde{X}(k) \cdot e^{j \cdot k \cdot i} dk\right] \\ \text{and } d(i) =& \frac{R}{V} \int_{-\infty}^{+\infty} D(k) \tilde{X}(k) \cdot e^{j \cdot k \cdot i} dk. \end{aligned} \tag{20}$$

The R/V ratio defines an intrinsic parameter of the data acquisition as it relates the radial distance from the satellite to the ground to the speed of the spacecraft. The SAR Volterra kernel expression is achieved by expanding the relationship between the sea surface Fourier coefficients $\tilde{X}(k)$ and the SAR Fourier coefficients $\tilde{X}_{\mathrm{sar}}(k)$ on the polynomial basis. By expanding (20), into (21) shown at the bottom of the next page and by comparing this result and the theoretical Volterra kernels given in (13), the SAR Volterra kernels can be identified as

$$\begin{aligned} H_n(k_1, \ldots, k_n) =& \frac{\left(j \cdot k_x \frac{R}{V}\right)^n D(k_1) \ldots D(k_n)}{n!} \\ &+ \frac{\left(j \cdot k_x \frac{R}{V}\right)^{n-1} T^{\mathrm{rar}}(k_1) D(k_2) \ldots D(k_n)}{(n-1)!}. \end{aligned} \tag{22}$$

Using this expansion, we obtain the same results as Hasselmann and Hasselmann [9]. The SAR spectrum is found to be the sum of an infinite number of terms implying the cross correlation between the RAR image and the displacement field and the autocorrelation of the displacement field. This result on the SAR spectrum can also be retrieved by directly expanding the SAR spectrum (7), thus explaining the increase in the spectral tails due to higher order nonlinearity as already reported by Krogstad *et al.* in [15]. For discrete space formalism, azimuth smearing is not included in the kernel of (22) (the orbital velocity being uniform inside the sampled cell resolution), and must be taken into account by multiplying all the Volterra kernels of (22) by a coefficient $e^{-k_x^2 \cdot M_X^{dd}(0)/2}$. The spectrum show then a decrease equal to $e^{-k_x^2 \cdot M_X^{dd}(0)}$. This modeling of the Azimuth Smearing agrees with the loss in resolution for the bispectrum, since $-((k_x^1)^2 + (k_x^2)^2 + (k_x^1 + k_x^2)^2) \cdot M_X^{dd}(0)/2 =$

$$\begin{aligned} B_2(k_1, k_2) =& B_{2,1,1}(k_1, k_2) + B_{2,2,2}(k_1, k_2) \\ =& H_1(k_1) \cdot H_1(k_2) \cdot H_2^*(k_1, k_2) \cdot E\left\{\left|\tilde{X}(k_1)\right|^2 \cdot \left|\tilde{X}(k_2)\right|^2\right\} \\ &+ H_1(k_1) \cdot H_1^*(k_1 + k_2) \cdot H_2(-k_1, k_1 + k_2) \cdot E\left\{\left|\tilde{X}(k_1)\right|^2 \cdot \left|\tilde{X}(k_1 + k_2)\right|^2\right\} \\ &+ H_1(k_2) \cdot H_1^*(k_1 + k_2) \cdot H_2(-k_2, k_1 + k_2) \cdot E\left\{\left|\tilde{X}(k_2)\right|^2 \cdot \left|\tilde{X}(k_1 + k_2)\right|^2\right\} \\ &+ \int_{-\infty}^{+\infty} H_2(-k_2 + k_j, k_1 + k_2 - k_j) \cdot H_2(k_j, k_2 - k_j) \cdot H_2^*(k_j, k_1 + k_2 - k_j) \\ &\cdot E\left\{\left|\tilde{X}(k_2 - k_j)\right|^2 \cdot \left|\tilde{X}(k_1 + k_2 - k_j)\right|^2 \cdot \left|\tilde{X}(k_j)\right|^2\right\} dk_j \end{aligned} \tag{18}$$

$-((k_x^1)^2+(k_x^2)^2+k_x^1\cdot k_x^2)\cdot M_X^{dd}(0)$ which is the decrease of resolution of the bispectrum (8).

IV. Theoretical Results

In order to validate the SAR expansion using Volterra models, we computed the spectral and bispectral distances between Volterra models of different orders and the complete SAR transform of (1). The spectrum and the bispectrum of the complete transform were computed using expression (7) and (8), respectively. The SAR spectrum and the bispectrum of the SAR Volterra models were computed by introducing the expression of the Volterra models (12), using the kernels deduced from the SAR transform (22) in the spectrum definition (2). Similarly, the bispectrum was computed by introducing the SAR kernels in definition (5). We also estimated the spectrum and bispectrum by averaging the Fourier Transform of simulated images. Since results are quite close we only display the theoretical ones. Tests were performed for values of the significant waveheight H_s equal to 3, 5, 7, and 9 m, and the wavelength values were chosen to be 100, 200, and 500 m with the angle of propagation with respect to the range axis being between 0° and 90°. The radar parameters, especially the incidence angle and the R/V ratio, were set to be equal to the ERS-1 parameters (i.e., an incidence angle of 23° and $R/V=115$). Because our goal is to compare several stochastic processes (the complete SAR transform and its approximation by Volterra models) with an underlying physical process, we chose the spectral distance between a spectrum $S_1(k)$ and a spectrum $S_2(k)$ to be:

$$\Delta S=\sqrt{\int_{-\infty}^{+\infty}|S_1(k)-S_2(k)|^2\,dk} \tag{23}$$

among all the possible definitions of spectral distance collected by Basseville in [6]. Moreover, in order to better understand the SAR spectrum shape and the order of the nonlinear interactions involved in this shape we defined the spectrum weight of the interactions of order p and order q [see (15)] as

$$W_{p,q}=100\cdot\frac{\int_{-\infty}^{+\infty}S_{p,q}(k)dk}{\int_{-\infty}^{+\infty}S_N(k)dk}. \tag{24}$$

The collection of weights of the different subspectra of a spectrum of a Volterra model of order N (defined in (24)) is called the "energy distribution". Similar to the spectral distance, we define the bispectral distance between a bispectrum $B_1(k_1,k_2)$ and a bispectrum $B_2(k_1,k_2)$ as

$$\Delta B=\sqrt{\int_{-\infty}^{+\infty}\int_{-\infty}^{+\infty}|B_1(k_1,k_2)-B_2(k_1,k_2)|^2\,dk_1dk_2}. \tag{25}$$

The next two sections give deeper insight into the approximation of the SAR transform by Volterra models. Section IV-A presents the spectral comparison between the spectrum of the complete SAR transform and the spectra of Volterra models of different orders whilst Section IV-B gives some results derived from nonlinearity indices and bicoherence tables.

A. Spectral Analysis

Figs. 2–5 present the spectral and bispectral distances in decibels and "energy distribution" for a wavelength of 200 m, and for significant waveheights of $H_s=3,5,7$, and 9 m. Figs. 7–12 present the spectra of a complete SAR transform (used as the reference) and Volterra models up to the fifth order. The contribution of each kernel can be deduced by comparing different Volterra model spectra as discussed in this section. We present these configurations because the SAR transform changes from a quasi-linear behavior to a strongly nonlinear one as explained below. For these results, we can formulate the following six conclusions.

- The cross spectra $S_{p+2,p}(k)$, such as the linear-cubic spectrum or the quadratic-tetric spectrum, are negative (as seen in the energy distribution of Figs. 2–5 since $W_{3,1}$ and $W_{4,2}$ are negative for all cases). This is logical since the interactions of orders $p+2$ and p are in phase opposition (due to j in the exponential expansion; see (22)). This remark explains (with some other reasons detailed below) why interactions of orders greater than three do not contribute strongly to the SAR spectrum shape (as seen below) since $S_{p,p-2}(k)$ and $S_{p,p}(k)$ cancel each others out as seen, for instance, in the symmetry of $W_{3,3}$ and $W_{3,1}$ or $W_{4,4}$ and $W_{4,2}$ of the energy distribution in Figs. 2–5.
- For common sea states, i.e., H_s smaller than 5 m and wavelengths greater than 200 m, the SAR process is widely dominated by the linear kernel (see $W_{1,1}$ in the energy distribution in Fig. 2). In the spectral distance of Fig. 2, there are few improvements produced by higher

$$\begin{aligned}\tilde{X}_{\mathrm{sar}}(k)=\sum_i\Bigg(\sum_{n=0}^{+\infty}\frac{1}{n!}\sigma_0\Bigg[\left(j\cdot\frac{R\cdot k_x}{V}\right)^n&\\ \cdot\int_{-\infty}^{+\infty}\cdots\int_{-\infty}^{+\infty}D(k_1)\ldots D(k_n)\cdot\tilde{X}(k_1)\ldots\tilde{X}(k_n)\cdot e^{j\cdot i\cdot(k_1+\cdots+k_n)}dk_1\ldots dk_n&\\ +\left(j\cdot\frac{R\cdot k_x}{V}\right)^n\int_{-\infty}^{+\infty}\cdots\int_{-\infty}^{+\infty}T^{\mathrm{rar}}(k_0)\ldots D(k_n)\cdot\tilde{X}(k_0)\ldots\tilde{X}(k_n)&\\ \cdot e^{j\cdot i\cdot(k_0+k_1+\cdots+k_n)}dk_0\cdots dk_n\Bigg]\Bigg)\cdot e^{-j\cdot k\cdot i}&\end{aligned} \tag{21}$$

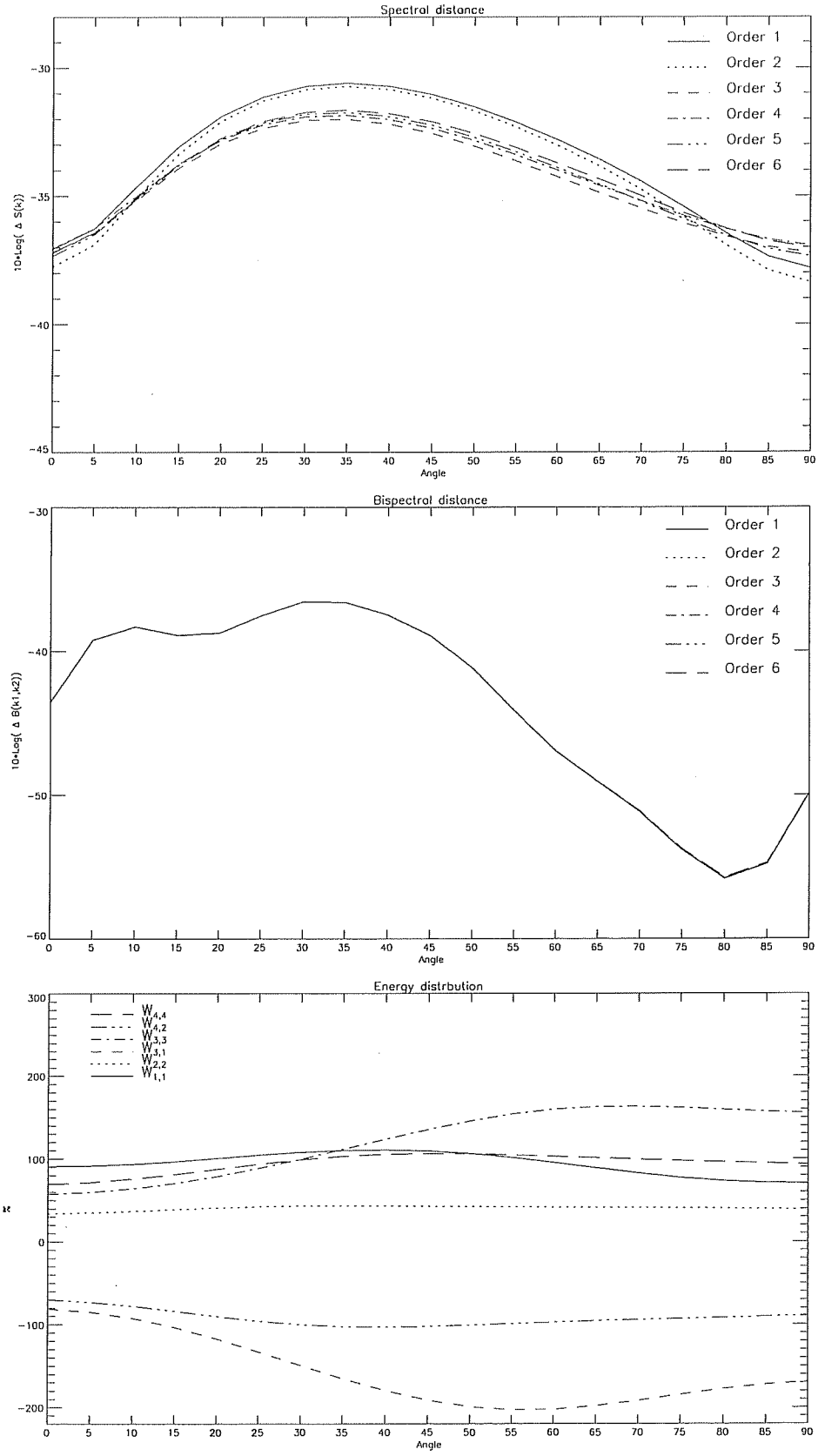

Fig. 2. Spectral and bispectral distances and energy distribution for $H_s = 3$ and a wavelength of 200 m.

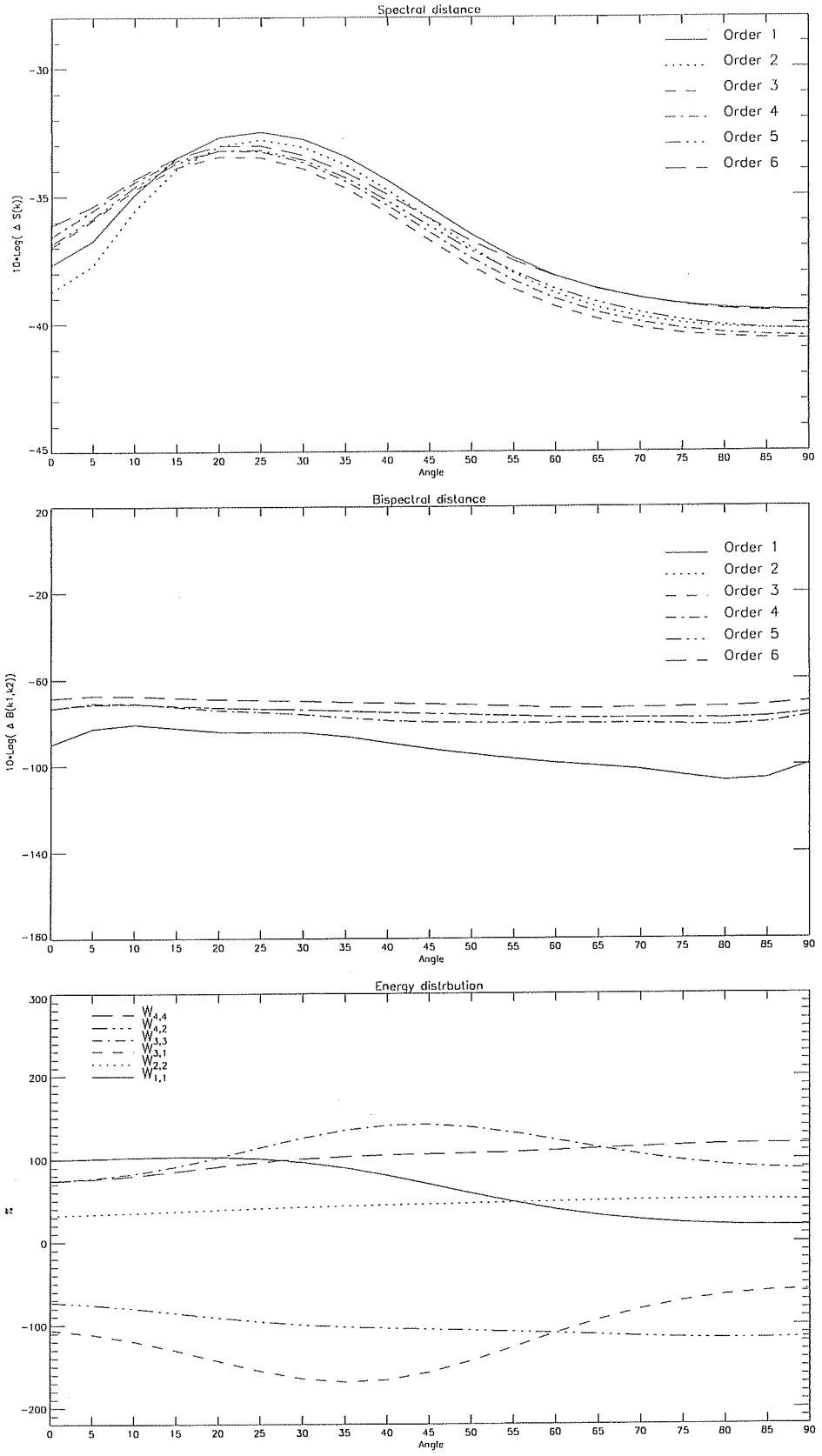

Fig. 3. Spectral and bispectral distances and energy distribution for $H_s = 5$ and a wavelength of 200 m.

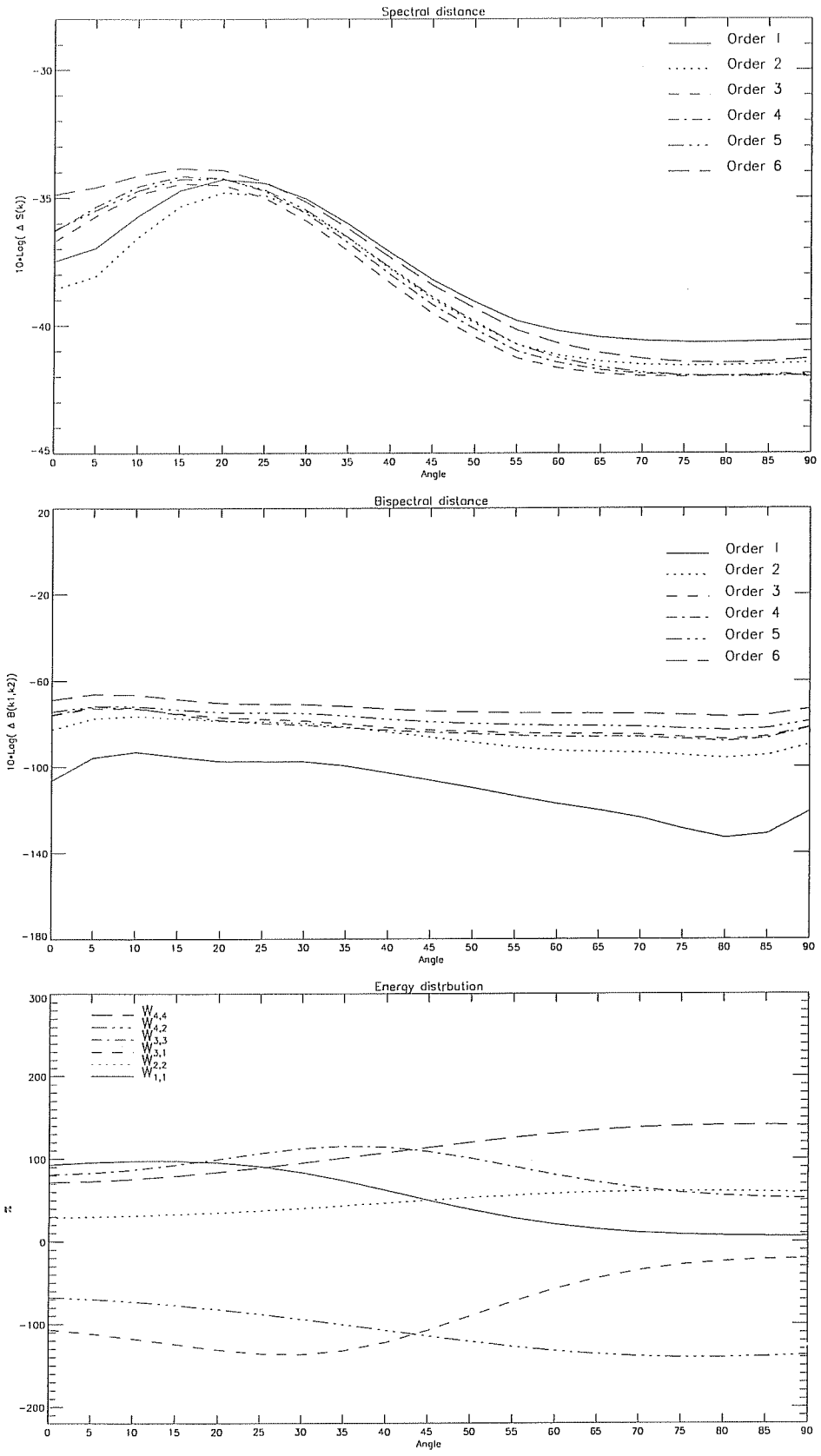

Fig. 4. Spectral and bispectrai distances and energy distribution for $H_s = 7$ and a wavelength of 200 m.

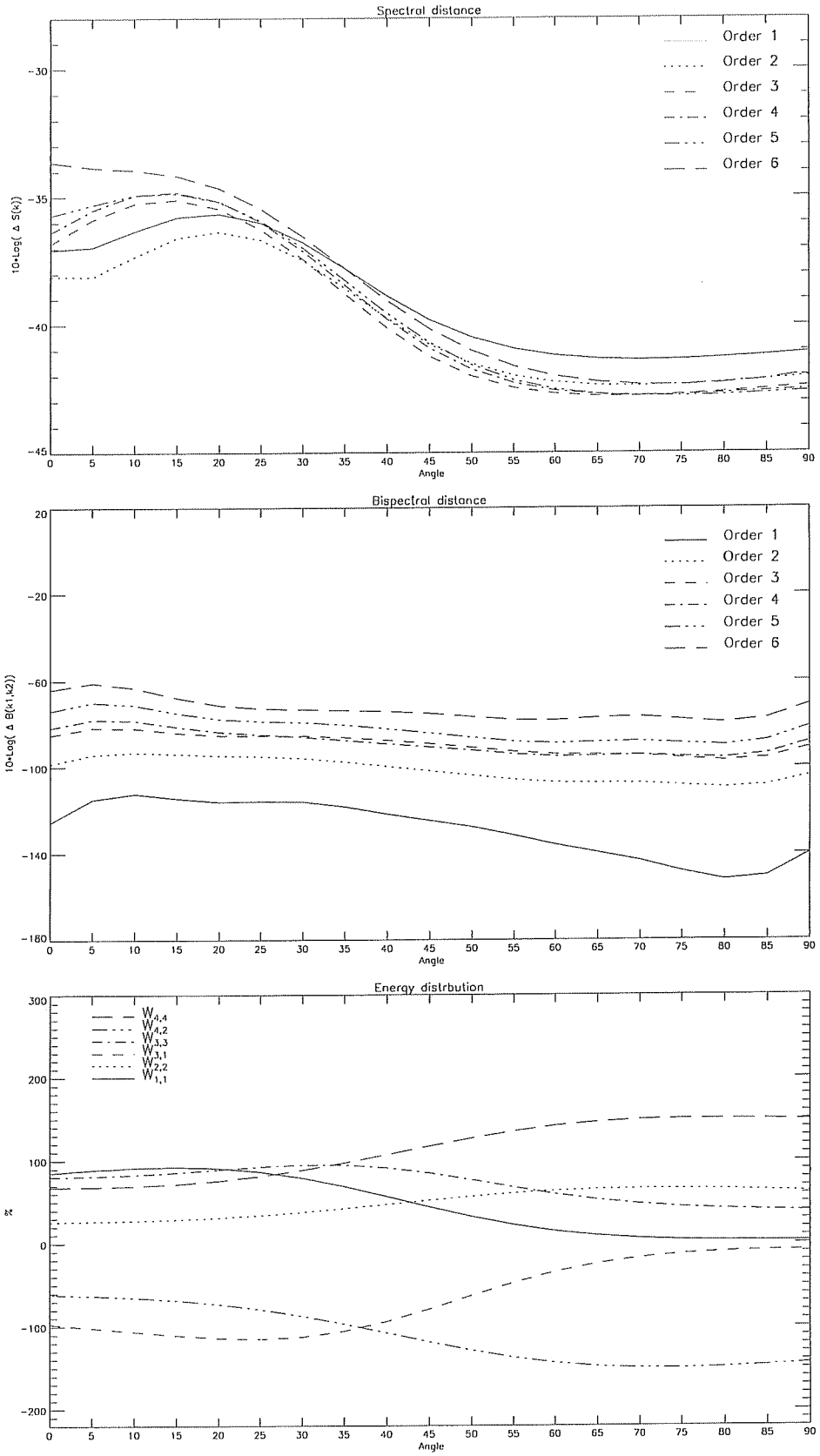

Fig. 5. Spectral and bispectral distances and energy distribution for $H_s = 9$ and a wavelength of 200 m.

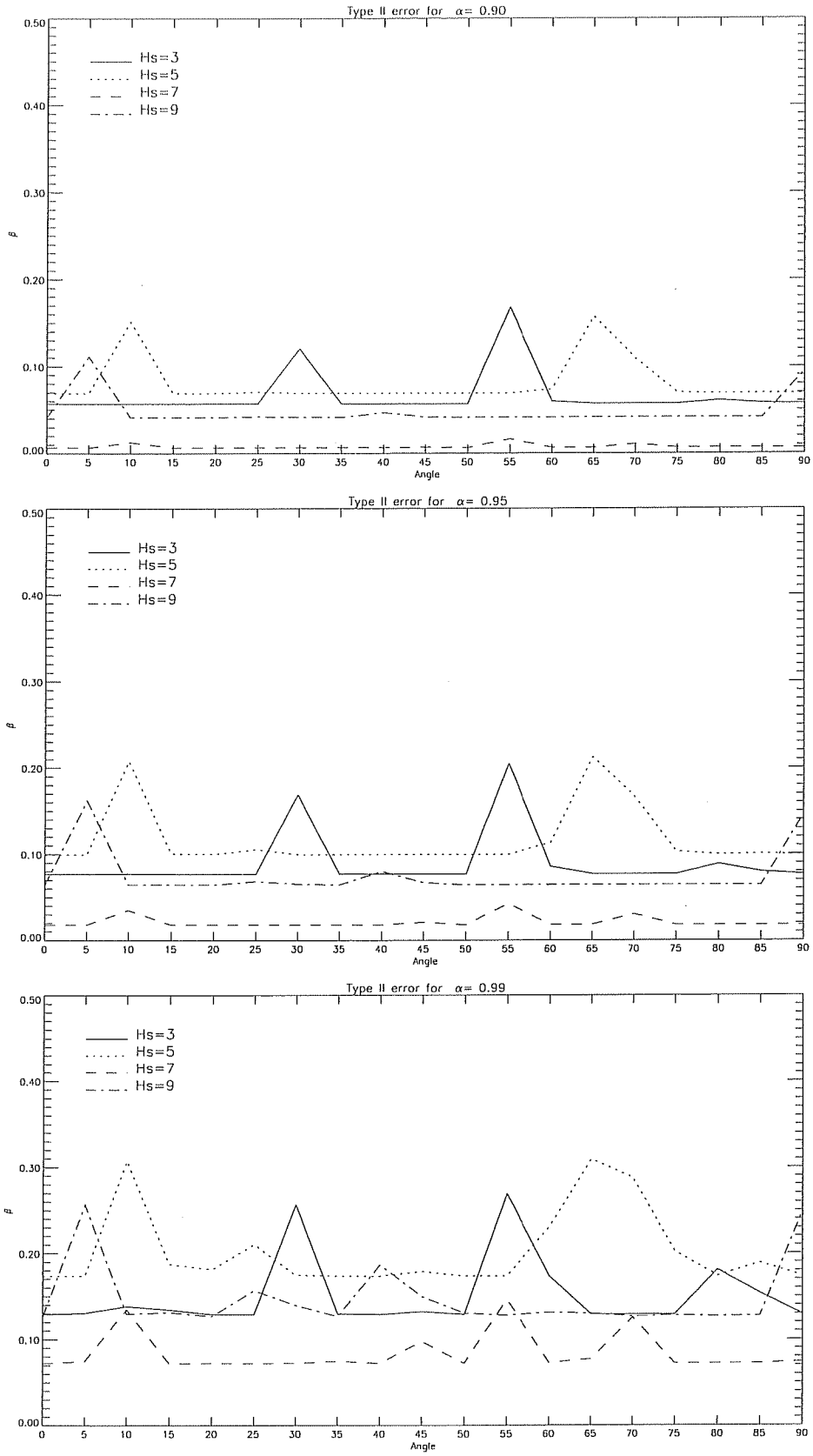

Fig. 6. Second error type β for $\alpha = 0.9$, $\alpha = 0.95$, $\alpha = 0.99$.

order kernels since all the spectral distance curves are quite close as depicted in Fig. 2. However, the corrections due to the cubic kernel cannot be neglected and, even if they are weak, they contribute to the decrease of spectral peaks which are stronger in the FOVM spectrum than in the SAR spectrum [see Fig. 7(a) and (b)].

- For high sea states, we can see a behavior change, since the spectrum turns from a linear mode observed for small dominant wave direction angles (below 55° for $H_s = 5$ and below 45° for $H_s = 7$, $H_s = 9$) to a quadratic mode. Equivalent linear and quadratic spectra exist for a narrow range of angles generally centered around 45°, as seen in Figs. 9 and 10. In fact, for all these sea states, the SAR spectrum shape is very close to the SOVM shape while the FOVM spectrum is almost null [compare Fig. 11(a), (b), and (c)]. Moreover, as seen in Figs. 4 and 5, the weight of the linear spectrum ($W_{1,1}$) decreases to zero while the quadratic spectrum ($W_{2,2}$) is close to 100. This quasi-bimodal behavior, which passes within a small range of angles from a linear mode to a quadratic mode, can be explained by two competitive phenomena. They are as follows.
  1) When the original spectrum is closer to the azimuth axis, more quadratic interactions are created. The quadratic spectrum is located on a strip in the azimuth direction. The high azimuthal components are eliminated by azimuth smearing (so there are few constructive quadratic interactions in the SAR process) while the low azimuthal quadratic components are removed due to the factor $(k_x)^2$ in the quadratic kernel (see (22) for $n = 2$). This low–high quadratic component removal explains the shape of the destructive quadratic interaction spectrum which is divided into almost symmetrical spectra (Figs. 11 and 12) and presents a large bandwidth in the range direction (see Figs. 9–12). Consequently, a large range bandwidth (or as mentioned by some authors, "cigar" shape [5]) is characteristic of the quadratic mode.
  2) The linear components are removed by azimuth smearing as the propagation angle increases. See for instance, Fig. 9, in which the dominant wave in the linear spectrum has an angle of 20° (while the input spectrum propagation angle was 45°) and thus seems to have turned toward the range axis (this point is retrieved even when the SAR process is linear). We note that azimuth smearing is a nonlinear phenomenon, but does not produce interactions. Therefore, this phenomenon is not detectable nor quantifiable by HOS methods.
- Higher order nonlinearities are also limited in a strip since low azimuthal components are eliminated by $(k_x)^n$ and high azimuthal components are removed by the azimuth smearing. The contributions of these interactions are then located in the SAR spectrum "basis" (i.e., the small spectrum values located over all the frequency plane [see Figs. 7(a), 9(a), 11(a)]. This explains why these nonlinearities, even if they do not contribute to the SAR spectrum shape, are not necessary negligible.
- As already noted [9], [14], the predominant phenomenon is so-called Velocity Bunching, which defines the shape of the SAR spectrum. The RAR modulation thus contributes to spectral asymmetries with regard to the range axis. As explained by Hasselmann and Hasselmann [9] for the quasi-linear transform (Figs. 7 and 8), the two spectral peaks are not strictly symmetrical. The phenomenon is also present for the quadratic kernel, the quadratic spectrum not being symmetrical with regards to the azimuthal axis (Figs. 9–12). A process solely dominated by the velocity bunching interactions could not lead to such asymmetries.
- A final conclusion, drawn from those above, is that the SAR spectrum shape is generally given by the linear Volterra kernel spectrum and in some cases by the quadratic kernel spectrum. The contribution of higher order interactions is mainly located in the spectrum basis and is sensitive up to the tenth order (for higher orders the corrections are negligible). This latter result thus gives an idea of the possible truncation order for an acceptable approximation of the SAR process by Volterra models and consequently gives a first design for the possible post-inverse Volterra model (not discussed in this paper).

B. Bispectral and Nonlinearity Analysis

The nonlinearity analysis was performed for three cases: a linear one (with $H_s = 7$ m, a wavelength of 200 m and an angle of 0°), a mixed case with both a linear spectrum and a quadratic one ($H_s = 7$ m, a wavelength of 200 m and an angle of 45°), and a quadratic case ($H_s = 7$ m, a wavelength of 200 m and an angle of 90°). The SAR spectrum decompositions for these three cases are depicted in Figs. 7–12, respectively, with the Volterra model spectrum up to the fifth order.

- The calculated bispectrum values [using (8)] are quite small and consequently the deduced values of the bicoherence [using (6)] are also small. The Volterra model bispectrum [using (17)] and bicoherence [using (6)] values are generally much greater. For this reason, the bispectrum closest to the SAR bispectrum is generally the FOVM bispectrum which is null (see Figs. 2–5). Moreover the bispectral distance increases with the Volterra model order and we have to add high order interactions for converging to the SAR bispectrum. As a first conclusion we can state that, even if the higher order interactions do not contribute strongly to the spectrum shape, their contribution is more important for the bispectrum. However, the bispectrum of SOVM is also quite close to the SAR bispectrum and the approximation of the SAR transform by a SOVM is then most valid for Volterra kernel identification by the methods cited in the introduction [13], [17], [20], [25].
- Results on the nonlinearity detection by the statistical index of Subba Rao and Gabr [27] are quite satisfactory since the Type II Error probability β is generally below 0.1 for $\alpha = 0.9$ and below 0.2 for $\alpha = 0.99$ (see Fig. 6).

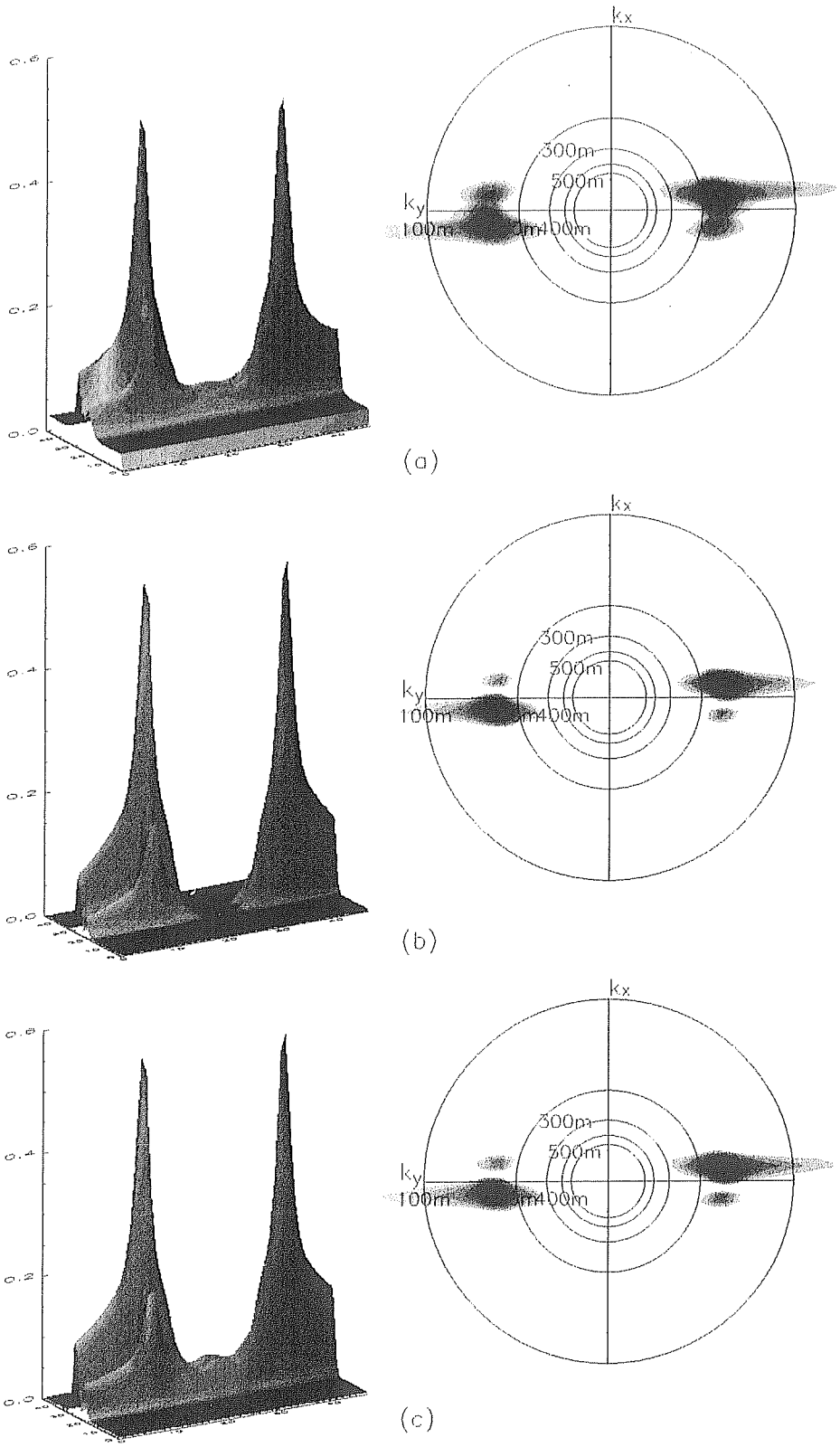

Fig. 7. (a) Spectrum of the complete SAR transform; (b) Volterra model of order 1; (c) Volterra model of order 2; for swell propagating along the range axis ($Hs = 7$ m and for a wavelength of 200 m).

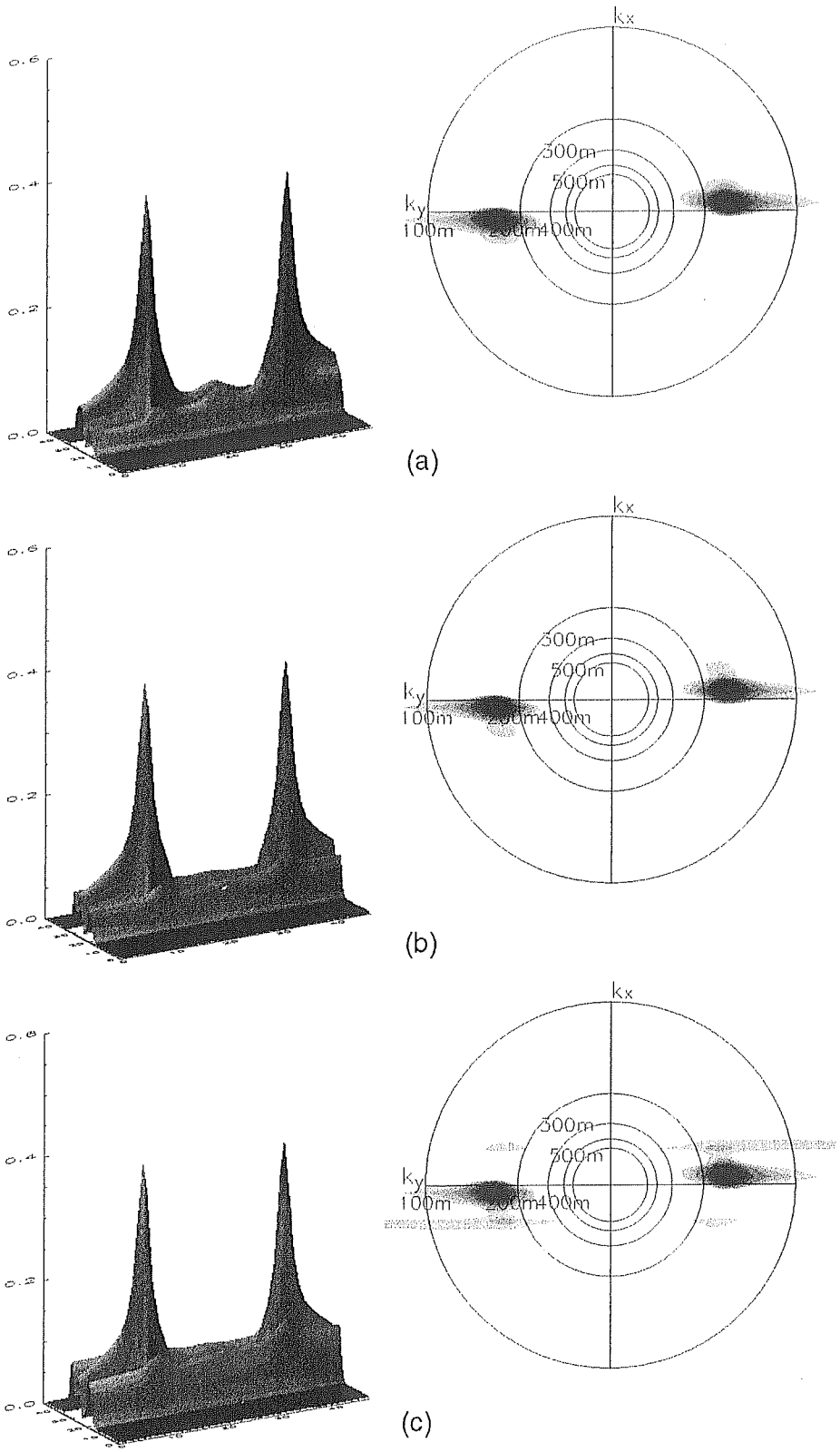

Fig. 8. (a) Spectrum of Volterra model of order 3; (b) Volterra model of order 4; (c) Volterra model of order 5; for swell propagating along the range axis ($Hs = 7$ m and for a wavelength of 200 m).

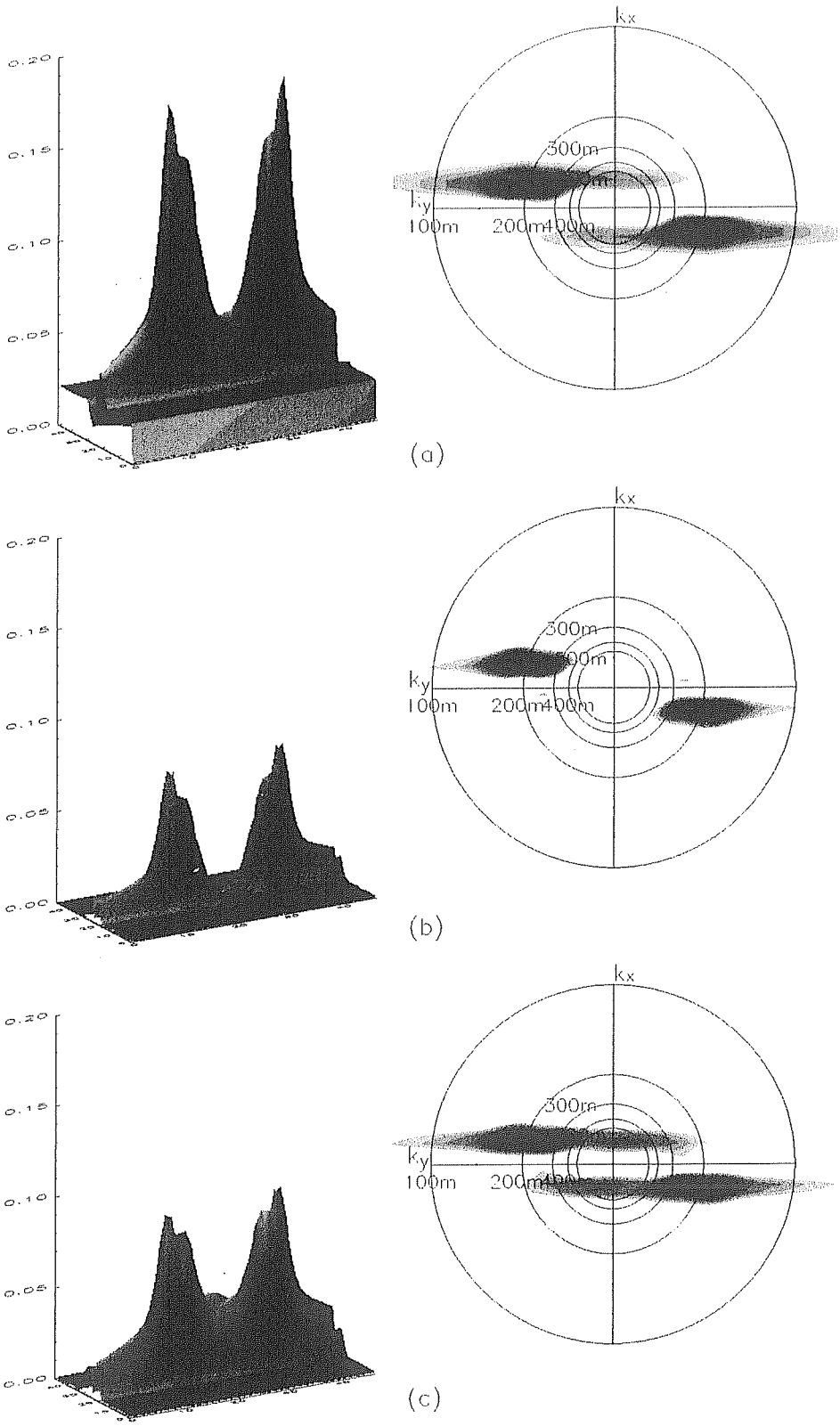

Fig. 9. (a) Spectrum of the complete SAR transform; (b) Volterra model of order 1; (c) Volterra model of order 2; for swell propagating with an angle of 45° with regards to the range axis ($Hs = 7$ m and for a wavelength of 200 m).

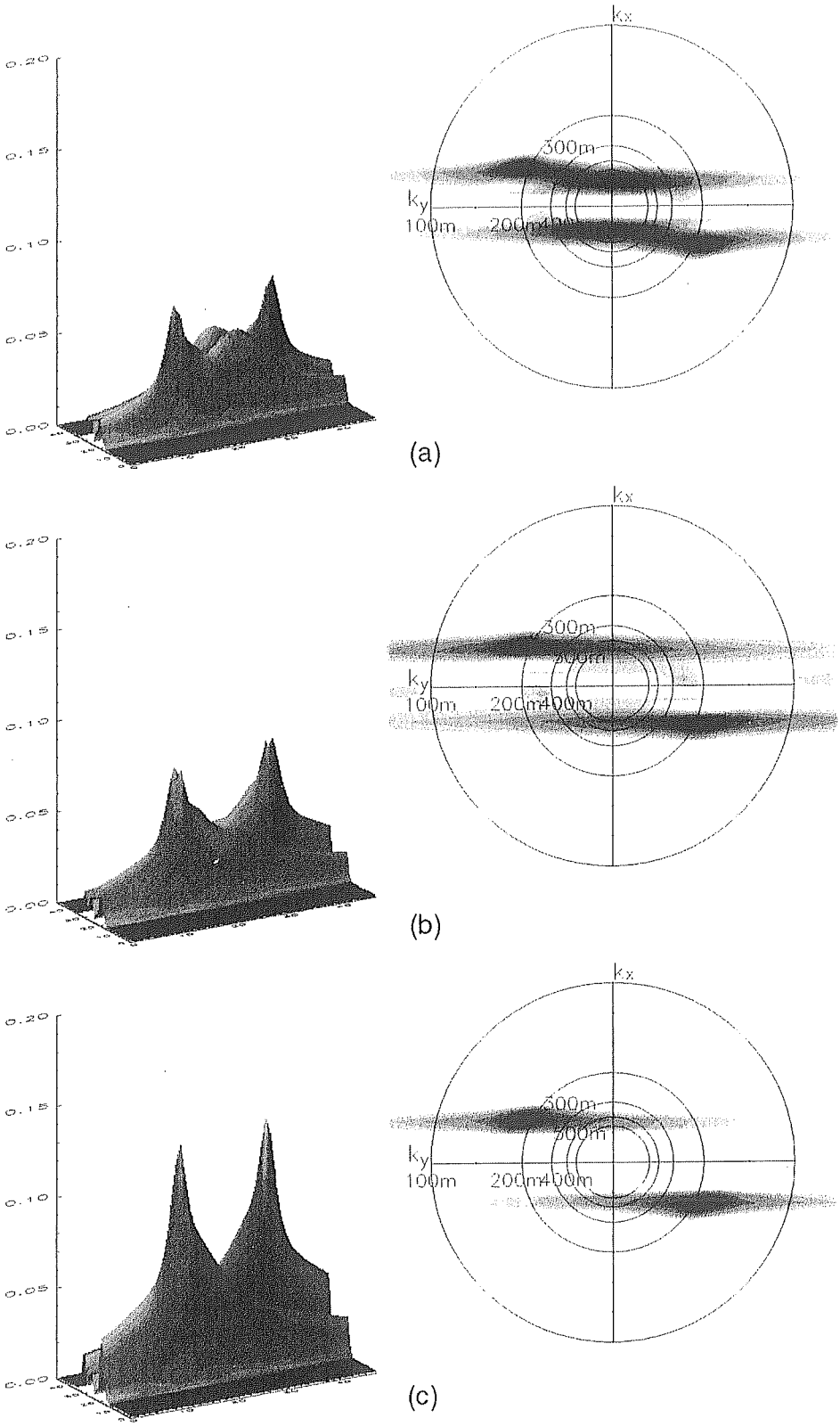

Fig. 10. (a) Spectrum of Volterra model of order 3; (b) Volterra model of order 4; (c) Volterra model of order 5; for swell propagating with an angle of 45° with regards to the range axis ($Hs = 7$ m and for a wavelength of 200 m).

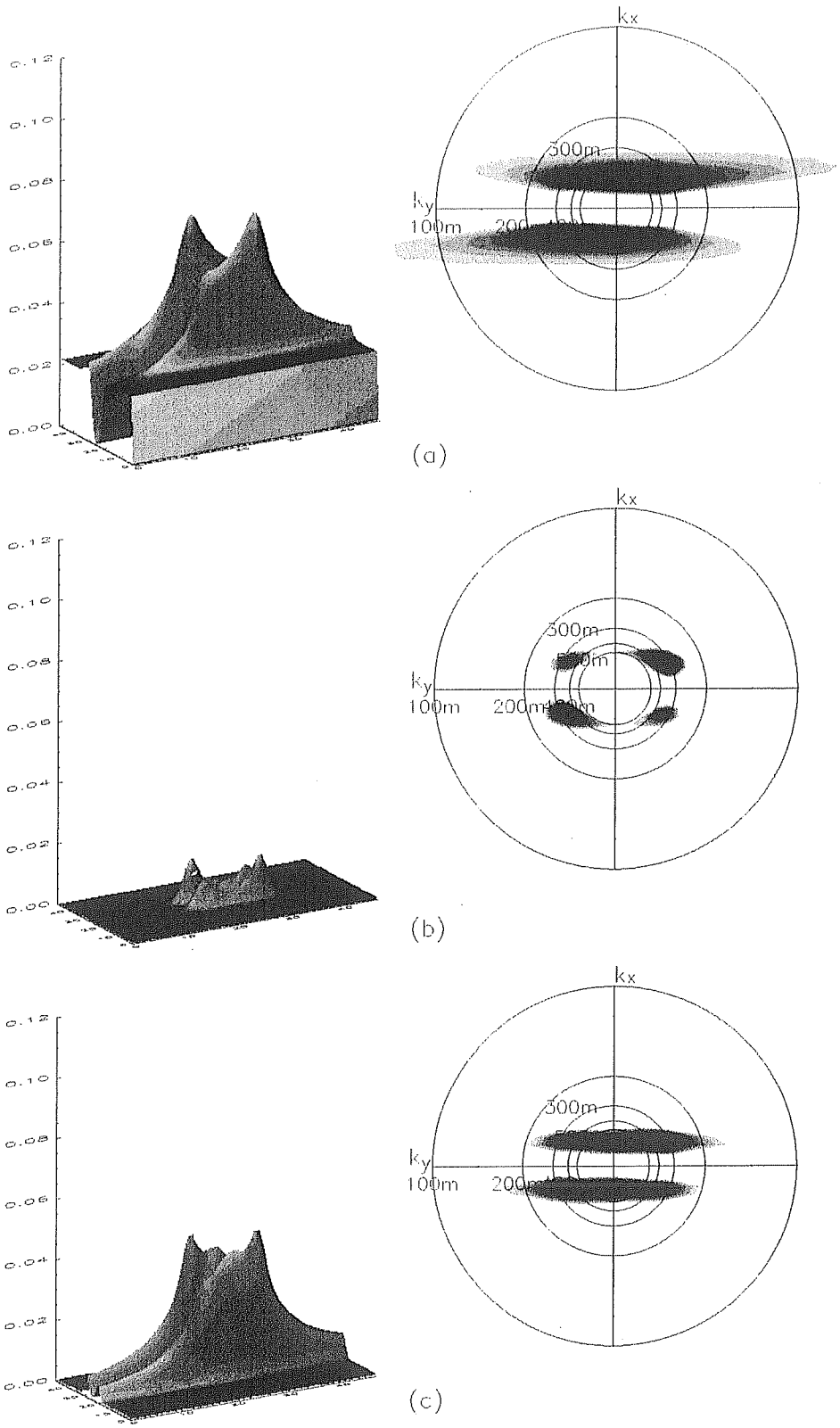

Fig. 11. (a) Spectrum of the complete SAR transform; (b) Volterra model of order 1; (c) Volterra model of order 2; for swell propagating along the azimuthal axis ($Hs = 7$ m and for a wavelength of 200 m).

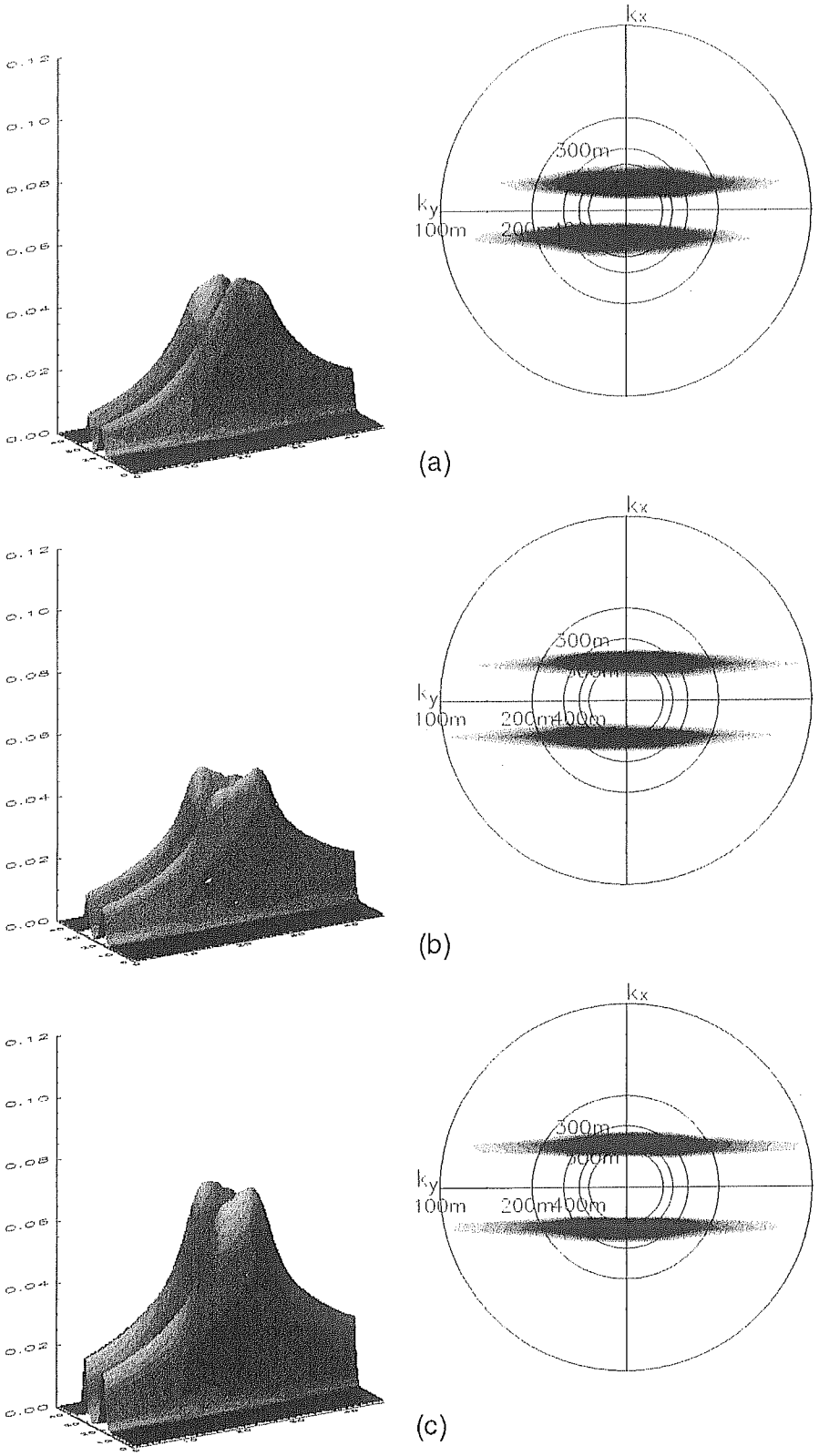

Fig. 12. (a) Spectrum of Volterra model of order 3; (b) Volterra model of order 4; (c) Volterra model of order 5; for swell propagating along the azimuthal axis ($Hs = 7$ m and for a wavelength of 200 m).

TABLE I
TYPE II ERROR PROBABILITY, FOR THE CST AND VOLTERRA MODEL UP TO THE SIXTH ORDER

	Linear mode	Mixed mode	Quadratic mode
CST	0.04	0.04	0.08
Order 2	0.10	0.10	0.10
Order 3	0.30	0.19	0.24
Order 4	0.28	0.40	0.28
Order 5	0.86	0.86	0.86
Order 6	0.50	0.53	0.59

An important point is that the classification between linear and nonlinear images does not depend on the nonlinearity energy since detection performance is quite good for both quasi-linear systems and for quadratic systems. Results of nonlinearity detection obtained on Volterra models are not as good although the bispectrum and the bicoherence values are stronger (see Table I). These values are quite similar and the bicoherence is flatter than the bicoherence of the SAR transform.

- Although bicoherence tables, tested on simulated images, are not a reliable tool for nonlinearity detection (due to the bicoherence variance estimation), they can provide a reliable location of the linear spectrum. Fig. 13 illustrates the linear spectrum location in the case of a mixed mode. The detection of the maximum values along the lines $k_x^1 = k_x^2$ and $k_y^1 = k_y^2$ leads to a linear component with a projection of about 150 m in the range direction and 600 m in the azimuth one. In Fig. 9(b), we verify that the "linear" spectrum is located at this wavenumber. However, the automatic linear spectrum determination, from the HBTs is not necessarily a trivial task, because linear and quadratic spectra can be connected (see Figs. 9 and 10) or the linear spectrum can be split (see Figs. 7 and 8).
- Nonlinearity quantification by using (19) is, in practice, the most difficult goal to achieve due to the high variance of the bicoherence estimates. Results obtained on simulated images give a nonlinear energy overestimation. Since the linear and the quadratic spectra are generally not located at the same place in the frequency domain, we can get around the quantification problem by simple location and delimitation of both spectra by using the results of Section IV-A under the restrictions noted above.

V. RESULTS ON ERS-1 IMAGES

The nonlinearity analysis method was tested for four ERS-1 (400 × 600) imagettes (the parameters are recalled in Table II). These imagettes were segmented into sixteen 128 × 128 subimagettes with some overlapping. The spectrum and bispectrum of the image were estimated by averaging $\tilde{X}(k) \cdot \tilde{X}^*(k)$ and $\tilde{X}(k_1) \cdot \tilde{X}(k_2) \cdot \tilde{X}^*(k_1 + k_2)$ calculated on each sub-image.

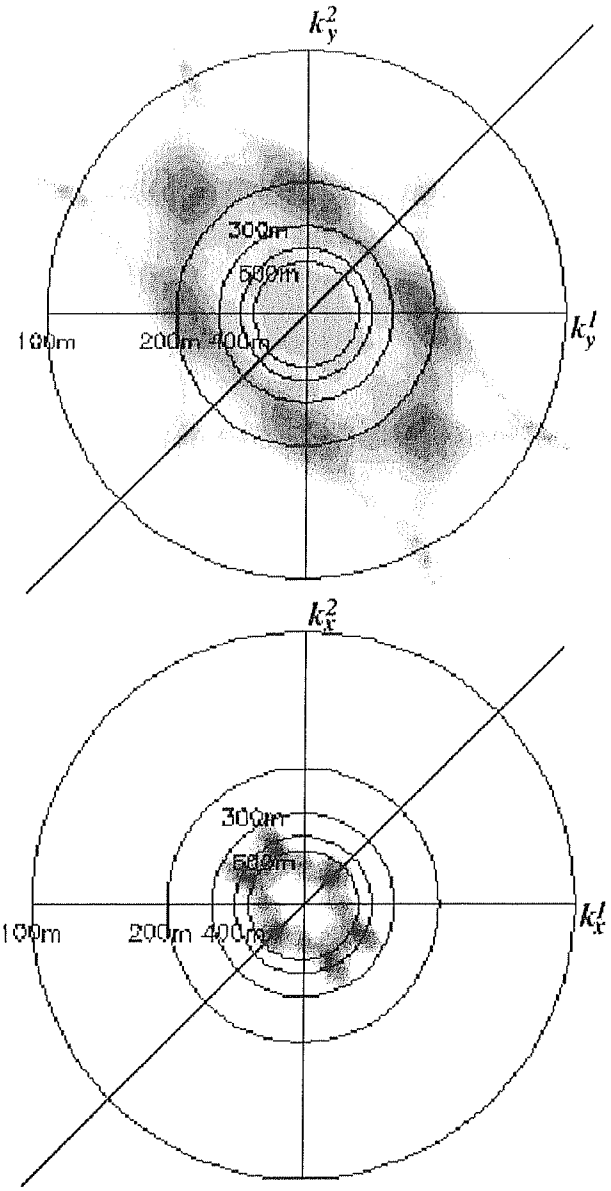

Fig. 13. HBTs for SAR simulated image, mixed mode (Range-Range top, Azimuth-Azimuth bottom).

TABLE II
ERS-1 IMAGE DATA: DAY, HOUR, LATITUDE, LONGITUDE, DOMINANT WAVELENGTH (DW), ESTIMATED AZIMUTH CUTOFE (ACO), ESTIMATED NONLINEARITY INDEX $\hat{q}_1$

Number	Day	Hour	Lat.	Long	DW	ACO	$\hat{q}_1$
1	6 Oct. 93	23:39:36	24.72	341.18	417	147	4.38
2	30 Sep. 93	23:35:27	50.62	336.80	68	246	6.42
3	29 Sep. 93	12:16:27	22.16	313.80	229	371	8.08
4	5 Oct. 93	0:41:02	18.34	326.81	226	593	9.31

Results on these real SAR images agree with both the spectral and bispectral calculations, and with the nonlinearity index calculation. Here, we present the spectrum, the CBT and in one

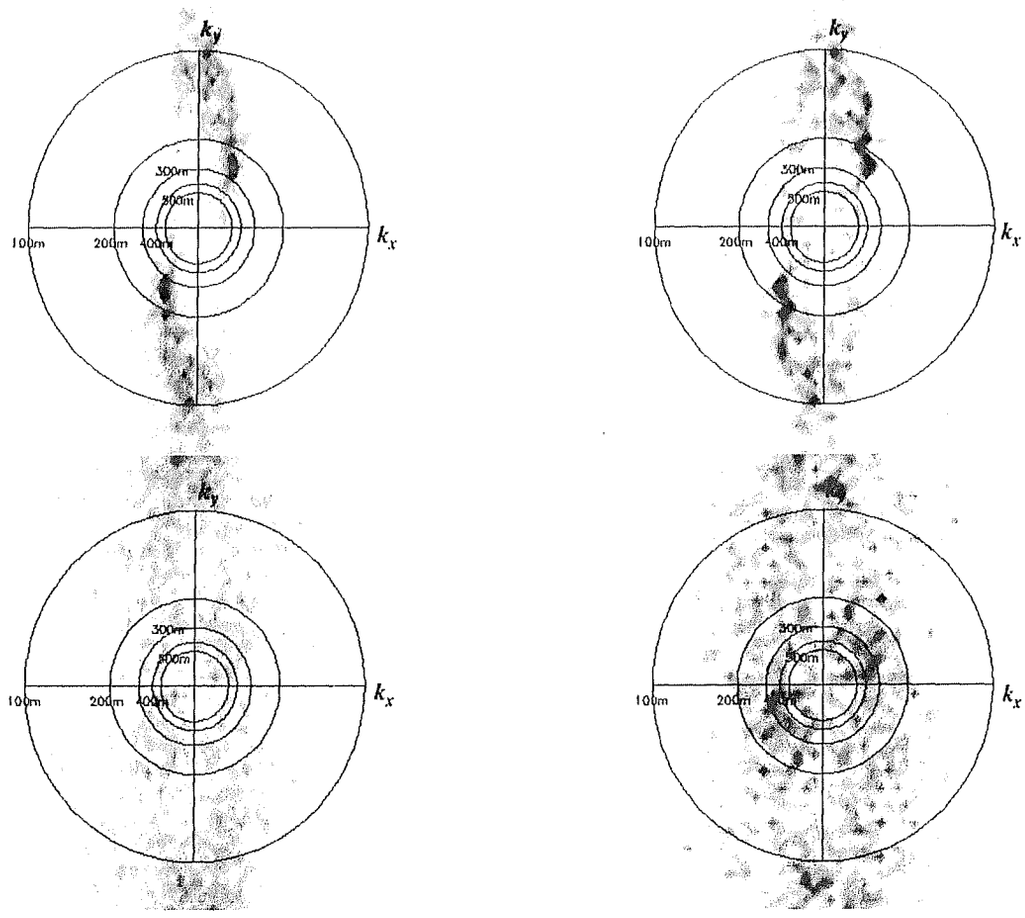

Fig. 14. Top: Spectrum and CBT for image 1. Bottom: Spectrum and CBT for image 2.

case the HBTs for these four images. The nonlinearity index estimates ($\hat{q}_1$) in Table II lead to a conclusion of linearity with a significance level $\alpha = 0.97$ (if $\hat{q}_1 < 5.693$ under the conditions given in Appendix A).

- The first image presents a spectrum with a narrow bandwidth in the azimuth direction (k_x), with a peak around 400 m (see Fig. 14) and the estimated azimuth cut-off around 100 m. The spectrum does not contain quadratic components (either scattered in the spectrum basis or located in a dominant quadratic spectrum). In the CBT representation (see Fig. 14), some components are darker than in the spectrum but this is due to bicoherence estimate variance rather than to nonlinearity detection. This image illustrates the case of a linear image of waves traveling in the azimuth direction, thus demonstrating that the SAR process for such a configuration can be linearly modeled.
- The second image has a dominant wavelength in the Range direction and the nonlinearity index leads to the conclusion of a nonlinear signal (see Table II). The comparison between the spectrum and the CBT (Fig. 14, second line) indicates stronger values (darker components) in the CBT for azimuthal components around 300 m, verifying the nonlinearity location along this axis as seen for simulated images. However, a nonlinear energy quantification by (19) leads to a low amount of nonlinear energy, thus proving that this image can also be considered as representative of the linear mode defined in Section IV-B.
- For the third image, the nonlinearity index also indicates a nonlinear signal, but the spectrum and the bicoherence table do not provide information about the nonlinearity location (all the Fourier components having nonlinearly interacted). From the HBTs of Fig. 15, we deduce that the linearly filtered original spectrum has a wavelength projection on the range axis around 150 and 500 m on the azimuth axis. Consequently, the spectral peak, in the 45° direction, is a quadratic artifact of the SAR process. This spectrum is close to the one of Fig. 9 for an original wave spectrum propagating in the 45° direction. We note that the quadratic kernel asymmetry is more important here than for the calculated spectra of Section IV-A, thus meaning that RAR modulation can be assumed to be different from the one used for our calculations.
- The fourth and last signal is also nonlinear according to the nonlinearity index (see Table II). The spectral tail (with regards to radial bandwidth) is unusually long. This tail can

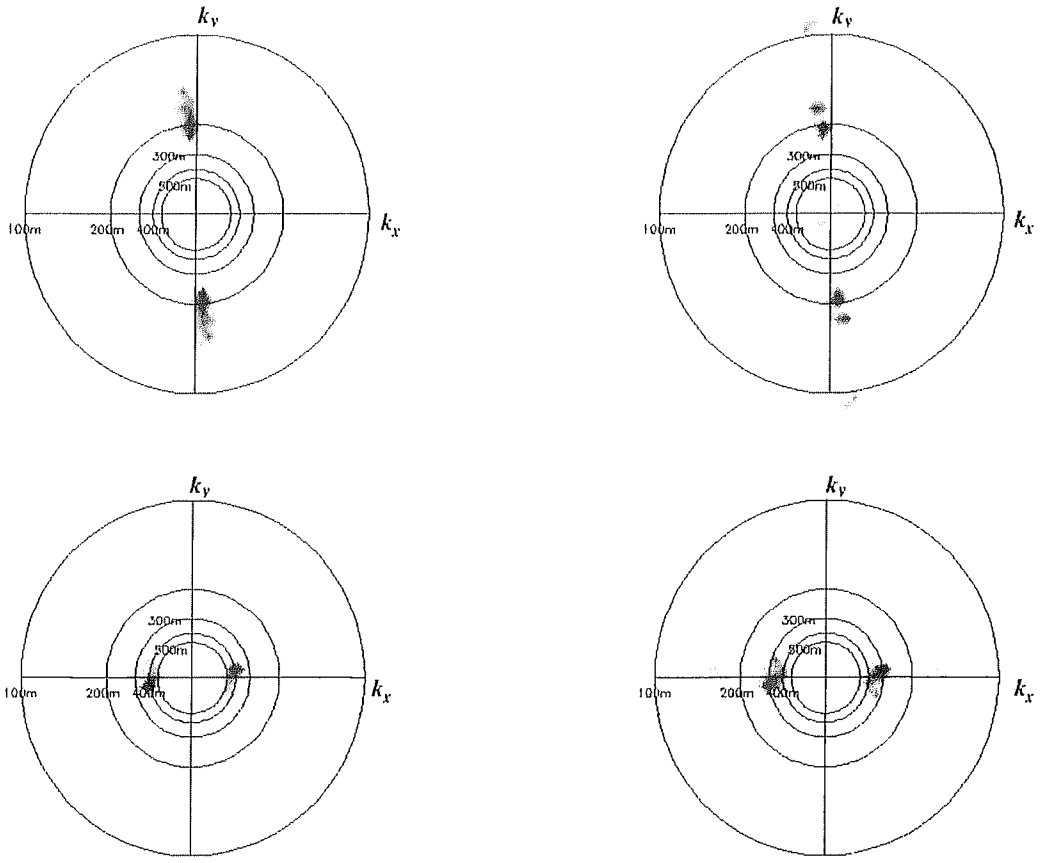

Fig. 14. *(Continued)* Top: Spectrum and CBT for image 3. Bottom: Spectrum and CBT for image 4.

be interpreted as constructive interactions, as verified on the HBTs. The fact that the spectrum is close to the range axis without spectrum splitting leads us to assume that the original spectrum has been compressed onto the range axis under Azimuth Smearing effects, a result verified by the high estimated azimuth cutoff (see Table II). We found a similar SAR spectrum for high H_s and for waves propagating with an angle of 30°, the proximity of the original wave spectrum to the range axis explains why no destructive quadratic interactions are detected. This image is an illustration of the nonlinearity quantification problem of Azimuth Smearing nonlinear effects, since SAR nonlinearities have not created nonlinear interactions for this image but have only filtered original components out. The image in Fig. 1 presents this kind of nonlinearity.

VI. Discussion and Conclusion

The results presented in this paper detail SAR transform modeling by a Volterra expansion for a better understanding of SAR spectral distortion. We show in this paper that the specific SAR mapping can be stated as being bimodal (either linear or quadratic). Tools derived from HOS, such as the nonlinearity index of Subba Rao and Gabr [27] or bicoherence tables, give fairly robust nonlinearity detection and location even if they are both disturbed by an intrinsic estimate variance problem (already reported by [7], [23], and [24]). This estimate variance prevents nonlinearity quantification. The tools used for nonlinearity location and detection assume Volterra modeling (up to the second order) and thus need the results of the decomposition of the SAR transform on Volterra models in order to give coherent results. A next step will be to use the Volterra model in the SAR inversion problem. But, in order to retrieve the sea spectrum from the SAR spectrum by post-inverse Volterra filtering, the direct linear kernel must not be null. This condition is not satisfied for the SAR linear kernel due to Azimuth Smearing. However, unlike linear systems, the loss of information by filtering (such as Azimuth Smearing) is not necessarily definitive for nonlinear systems. Indeed, the removed input Fourier components were somehow "recoded" by convolution of the quadratic kernel with other input Fourier components in the frequency domain, and could be recovered from this quadratic kernel. Thus the use of Volterra models, especially the SOVM, for SAR transform inversion, with a more sophisticated method, remains an open question.

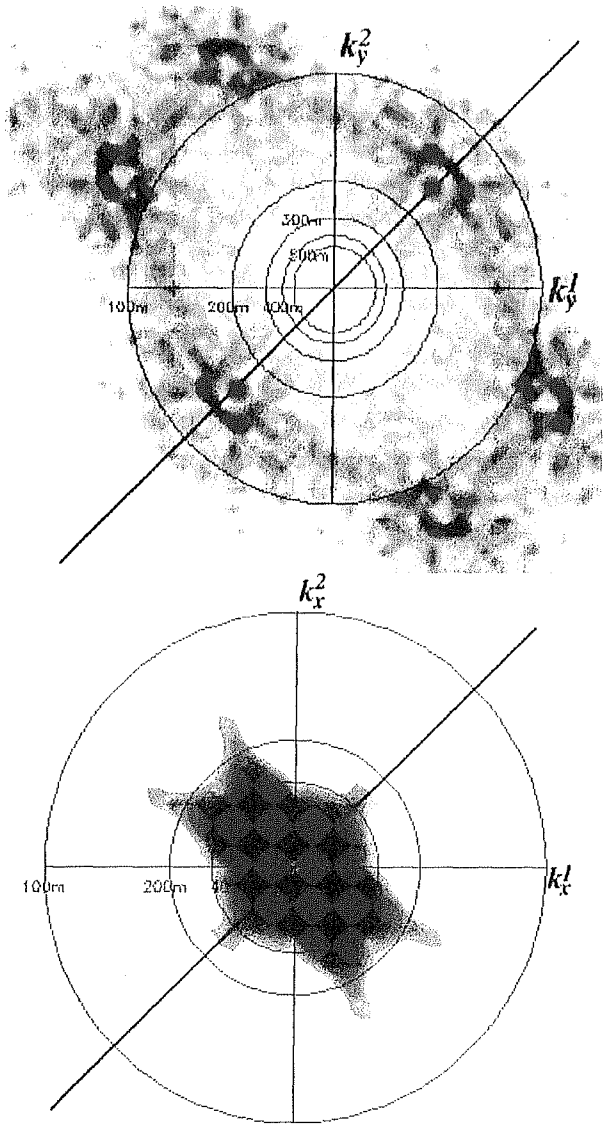

Fig. 15. HBTs for the third image (Top: Range–Range, Bottom: Azimuth–Azimuth).

APPENDIX I

In order to illustrate the mechanisms which have some effects on phase coupling detection, we consider the following signal:

$$X(n) = A_1 e^{j(k_1 \cdot n + \varphi_1)} + A_2 e^{j(k_2 \cdot n + \varphi_2)} + A_3 e^{j((k_1+k_2)\cdot n + \varphi_3)} + B \cdot e^{j((k_1+k_2)\cdot n + \varphi_1 + \varphi_2)} \tag{26}$$

where φ_i are random phases uniformly distributed over $[0, 2\pi]$. By using the bispectrum definition (5), we find that only the quadratically phase coupled part interferes in the bispectrum as $B(k_1, k_2) = E\{A_1 \cdot A_2 \cdot B\}/8$, while the spectrum is the sum of both components $S(k_1 + k_2) = E\left\{A_3^2 + B^2\right\}/4$. For general variables, the bicoherence expression does not lead to interesting results

$$P(k_1, k_2) = \frac{\left(E\{A_1 \cdot A_2 \cdot B\}\right)^2}{E\{A_1^2\} \cdot E\{A_2^2\} \cdot E\{A_3^2 + B^2\}} \tag{27}$$

but if we made the assumptions that $B = \alpha \cdot A_1 \cdot A_2$ and the A_i are independent Rayleigh variables (i.e., the input data are Gaussian), then the bicoherence gives the ratio of nonlinear energy over total energy at wavenumber $k_1 + k_2$

$$P(k_1, k_2) = \frac{E\{B^2\}}{E\{A_3^2 + B^2\}} = \frac{S_{qua}(k_1 + k_2)}{S(k_1 + k_2)}. \tag{28}$$

As seen in Section III, the assumption $B = \alpha \cdot A_1 \cdot A_2$ is verified for the second-order Volterra Model and the relation (28) is only valid for this model.

- Bicoherence being a 4-D structure, the information of the bicoherence is not immediately accessible for a global analysis. We thus propose to compress the bicoherence information, by summation along one of the three pairs of non redundant axes (k_x^1, k_x^2), (k_x^1, k_y^1), (k_y^1, k_y^2), into 2-D structures, the bicoherence tables. The bicoherence tables are consequently defined as (see [18])

$$\begin{aligned} T_{AA}(k_x^1, k_x^2) &= \int_{-\infty}^{+\infty}\int_{-\infty}^{+\infty} P(k_x^1, k_y^1, k_x^2, k_y^2)\, dk_y^1 dk_y^2 \\ T_{RR}(k_y^1, k_y^2) &= \int_{-\infty}^{+\infty}\int_{-\infty}^{+\infty} P(k_x^1, k_y^1, k_x^2, k_y^2)\, dk_x^1 dk_x^2 \\ T_{RA}(k_x^1, k_y^1) &= \int_{-\infty}^{+\infty}\int_{-\infty}^{+\infty} P(k_x^1, k_y^1, k_x^2, k_y^2)\, dk_x^2 dk_y^2. \end{aligned} \tag{29}$$

  The CBT, range-azimuth, $T_{RA}(k)$, gives the ratio of the total nonlinear energy over the total energy. In fact, by using (28) the complete quadratic energy is given by the sum of all quadratic interactions over the Fourier domain (i.e., for each pair of wavenumbers, the sum of which is equal to $k_1 + k_2$). The ratio of quadratic energy is given by $\int_{-\infty}^{+\infty} P(k_1 + k_2 - k_j, k_j) dk_j$. By bispectral symmetry [see definitions (5) and (6)], we obtain

$$\begin{aligned} &\int_{-\infty}^{+\infty} P(k_1 + k_2 - k_j, k_j)\, dk_j \\ &= \int_{-\infty}^{+\infty} P(k_1 + k_2, k_1 + k_2 - k_j)\, dk_j \\ &= \int_{-\infty}^{+\infty}\int_{-\infty}^{+\infty} P(k_x^1 + k_x^2, k_y^1 + k_y^2, k_x^j, k_y^j)\, dk_x^j dk_y^j \\ &= T_{RA}(k_1 + k_2) \end{aligned} \tag{30}$$

  and thus, the total quadratic energy is quantified by

$$S_{qua}(k_1 + k_2) = S(k_1 + k_2) \cdot T_{RA}(k_1 + k_2) \tag{31}$$

- The homogeneous tables ($T_{AA}\left(k_x^1, k_x^2\right)$ and $T_{RR}\left(k_y^1, k_y^2\right)$) have a different interpretation but they can be seen as the amount of energy between two waves, the azimuthal component of which is equal to k_x^1 and k_x^2 (k_y^1 and k_y^2, respectively). Especially, two harmonics of an original signal with a limited bandwidth spectrum have close wavenumber and their interactions are located in the homogeneous tables along the line $k_x^1 = k_x^2$ (respectively, $k_y^1 = k_y^2$). This property is useful for recovering the linearly filtered original spectrum location.
- The index proposed by Subba Rao and Gabr begins by choosing p values of different sample of the estimated bicoherence $\hat{P}(k_1, k_2)$ and forming the vector colon $\vec{Y} =$

$(Y_1, Y_2, \ldots, Y_p)^T$ and by constructing around each point (k_1, k_2) a fine frequency grid with

$$k_x^1\left(m_x^1\right) = k_x^1 + \frac{m_x^1 \cdot d \cdot \pi}{N} \quad k_y^1\left(m_y^1\right) = k_y^1 + \frac{m_y^1 \cdot d \cdot \pi}{N}$$
$$k_x^2\left(m_x^2\right) = k_x^2 + \frac{m_x^2 \cdot d \cdot \pi}{N} \quad k_y^2\left(m_y^2\right) = k_y^2 + \frac{m_y^2 \cdot d \cdot \pi}{N}$$

with

$$\begin{aligned} m_x^1 &= -J, -J+1, \ldots, 0, \ldots J-1, J \\ m_2^x &= -J, -J+1, \ldots, J-1, J \quad m_x^2 \neq 0 \\ m_y^1 &= -J, -J+1, \ldots, 0, \ldots J-1, J \\ m_y^2 &= -J, -J+1, \ldots, J-1, J \quad m_y^2 \neq 0 \end{aligned} \tag{32}$$

The distance d between the points must be chosen in such a way that:

$$E\left\{\hat{B}\left(k_x^1\left(m_x^1\right), k_y^1\left(m_y^1\right), k_x^2\left(m_x^2\right), k_y^2\left(m_y^2\right)\right)\right\} = B\left(k_1, k_2\right) \quad \forall\left(m_x^1, m_y^1, m_x^2, m_y^2\right) \tag{33}$$

see [27] or [10] for a discussion of this condition. We then obtain $n = 8J + 1$ trials $\vec{Y}_i$ of $\vec{Y}$. The problem is to test whether all the variables have the same mean and it is a well-known problem of symmetry addressed by Anderson in [3]. Since the mean of this value is not known, Subba Rao and Gabr define the $pX(p-1)$ matrix by

$$B = \begin{pmatrix} \mathrm{I} & -1 & 0 & 0 & \cdots & 0 \\ 0 & 1 & -1 & 0 & \cdots & 0 \\ \cdots & \cdots & \cdots & \cdots & \ddots & \cdots \\ 0 & \cdots & 0 & 0 & 1 & -\mathrm{I} \end{pmatrix} \tag{34}$$

and we calculate $\vec{Y} = B \cdot \vec{W}$. This array of variables is zero mean under the null hypothesis, i.e., the signal is linear. The remaining part of the test is based on the T^2 Hostelling test. It needs to introduce the variables

$$\bar{Y} = \frac{1}{n}\sum_{i=1}^{n} Y_i \quad \text{and} \quad \Sigma = \frac{1}{n}\sum_{i=1}^{n}\left(Y_i - \bar{Y}\right)\left(Y_i - \bar{Y}\right)^t \tag{35}$$

where t denotes the transposed matrix. The T^2 Hostelling statistics $T^2 = \bar{Y}\Sigma^{-1}\bar{Y}^t$, is then

$$\hat{q}_1 = T^2 \cdot \frac{(n-p+1)}{(p-1)} \tag{36}$$

and follows, under the null hypothesis, a central $F_{(p-1,n-p+1)}(x)$ distribution where $p-1$ and $n-p+1$ are the degree of freedom of the distribution. The central F distribution with p and $n-p$ degrees of freedom is given by

$$F^c(z) = \frac{1}{(n-1)\cdot\Gamma\left(\frac{n-p}{2}\right)} \cdot \frac{\left(\frac{z^2}{(n-1)}\right)^{p/2-1} \cdot \Gamma\left(\frac{n}{2}\right)}{\Gamma\left(\frac{p}{2}\right)\left(1+\frac{z^2}{(n-1)}\right)^{n/2-1}}. \tag{37}$$

Obviously, when the hypothesis H_0 is verified, T^2 is close to zero and this hypothesis is then accepted if T^2 is lower than any threshold z_0 determined by the significance level α.

$$\int_0^{z_0} F^c(z)dz = \alpha. \tag{38}$$

For instance, for $\alpha = 0.97$, with $n = 17$ and $p = 7$ (we use these values for the tests of Section IV-B) then $z_0 = 5.693$. When the signal is nonlinear $\hat{q}_1$ is a noncentral F distribution, the noncentrality parameter being

$$\tau^2 = \nu^t S^{-1} \nu \tag{39}$$

where ν is the true mean vector and S the true covariance matrix of random variable array $\vec{Y}$. The non central F-distribution (with noncentrality parameter τ^2 and p and $n-p$ degrees of freedom) is given by

$$F^{nc}(z) = \frac{e^{\tau^2/2}}{(n-1)\Gamma\left(\frac{n-p}{2}\right)} \sum_{i=0}^{+\infty} \frac{\left(\frac{\tau^2}{2}\right)^i \left[\frac{z^2}{(n-1)}\right]^{(1/2)p+i-1} \Gamma\left(\frac{n}{2}+i\right)}{i!\Gamma\left(\frac{p}{2}+i\right)\left[1+\frac{z^2}{(n-1)}\right]^{p/2+i}} \tag{40}$$

The type II error probability is thus given by

$$\beta = \int_0^{z_0} F^{nc}(z)dz \tag{41}$$

APPENDIX II

By applying the bispectrum definition (5) to the SAR expression of (1)

$$\begin{aligned} B_{\mathrm{sar}}&\left(k_1, k_2\right) \\ =& E\left\{\tilde{X}_{\mathrm{sar}}\left(k_1\right)\cdot\tilde{X}_{\mathrm{sar}}\left(k_2\right)\cdot\tilde{X}^*_{\mathrm{sar}}\left(k_1+k_2\right)\right\} \\ &- E\left\{\tilde{X}_{\mathrm{sar}}\left(k_1\right)\cdot\tilde{X}_{\mathrm{sar}}\left(k_2\right)\right\}\cdot E\left\{\tilde{X}^*_{\mathrm{sar}}\left(k_1+k_2\right)\right\} \\ &- E\left\{\tilde{X}_{\mathrm{sar}}\left(k_1\right)\cdot\tilde{X}^*_{\mathrm{sar}}\left(k_1+k_2\right)\right\}\cdot E\left\{\tilde{X}_{\mathrm{sar}}\left(k_2\right)\right\} \\ &- E\left\{\tilde{X}_{\mathrm{sar}}\left(k_2\right)\cdot\tilde{X}^*_{\mathrm{sar}}\left(k_1+k_2\right)\right\}\cdot E\left\{\tilde{X}_{\mathrm{sar}}\left(k_1\right)\right\} \\ &+ 2\cdot E\left\{\tilde{X}_{\mathrm{sar}}\left(k_1\right)\right\}\cdot E\left\{\tilde{X}_{\mathrm{sar}}\left(k_2\right)\right\} \\ &\cdot E\left\{\tilde{X}^*_{\mathrm{sar}}\left(k_1+k_2\right)\right\} \\ =& E\left\{\tilde{X}_{\mathrm{sar}}\left(k_1\right)\cdot\tilde{X}_{\mathrm{sar}}\left(k_2\right)\cdot\tilde{X}^*_{\mathrm{sar}}\left(k_1+k_2\right)\right\} \\ &- \sigma_0\cdot S_{\mathrm{sar}}\left(k_1\right)\delta\left(k_1+k_2\right) - \sigma_0\cdot S_{\mathrm{sar}}\left(k_2\right)\delta\left(k_1\right) \\ &- \sigma_0\cdot S_{\mathrm{sar}}\left(k_1\right)\delta\left(k_2\right) + 2\cdot\sigma_0^3\cdot\delta\left(k_1\right)\cdot\delta\left(k_2\right). \end{aligned} \tag{42}$$

Proceeding as Krogstad in [14], we have (43) shown at the bottom of the page. By applying the stationarity of

$$\begin{aligned} &E\left\{\tilde{X}_{\mathrm{sar}}\left(k_1\right)\cdot\tilde{X}_{\mathrm{sar}}\left(k_2\right)\cdot\tilde{X}^*_{\mathrm{sar}}\left(k_1+k_2\right)\right\} \\ &= |A|^{-3} \underset{|A|\to+\infty}{Lim} \int_{x\in A}\int_{x'\in A'}\int_{x''\in A''} E\left\{e^{j\cdot k_x^1\cdot(d(x')-d(x))}\cdot e^{j\cdot k_x^2\cdot(d(x'')-d(x))}\cdot X_{\mathrm{rar}}(x)\cdot X_{\mathrm{rar}}\left(x'\right)\cdot X_{\mathrm{rar}}\left(x''\right)\right\} \\ &\quad\cdot e^{-j\cdot k_1\cdot(x'-x)}\cdot e^{-j\cdot k_2\cdot(x''-x)}dx\cdot dx'\cdot dx'' \\ &= |A|^{-3} \underset{|A|\to+\infty}{Lim} \int_{x\in A}\int_{x'\in A'}\int_{x''\in A''} H\left(x, x', x'', k_x^1, k_x^2\right)\cdot e^{-j\cdot k_1\cdot(x'-x)}\cdot e^{-j\cdot k_2\cdot(x''-x)}dx\cdot dx'\cdot dx'' \end{aligned} \tag{43}$$

the sea surface up to the order 3, (43) can be rewritten as

$$E\left\{\tilde{X}_{\mathrm{sar}}(k_1)\cdot\tilde{X}_{\mathrm{sar}}(k_2)\cdot\tilde{X}^*_{\mathrm{sar}}(k_1+k_2)\right\} = |A|^{-2}\underset{|A|\to+\infty}{Lim}\int_{x\in A}\int_{x'\in A'} H\left(x,x',k_x^1,k_x^2\right)e^{-j\cdot k_1\cdot x}\cdot e^{-j\cdot k_2\cdot x'}dx\cdot dx'$$

with

$$H\left(x,x',k_x^1,k_x^2\right) = E\left\{X_{\mathrm{rar}}(x')\cdot X_{\mathrm{rar}}(x)\cdot X_{\mathrm{rar}}(0)e^{-j\cdot k_x^1\cdot\left(d(0)-d\left(x'\right)\right)}\cdot e^{-j\cdot k_x^2\cdot(d(0)-d(x))}\right\}.$$

This expression can be calculated by considering the six-element random array

$$X = \left(X_{\mathrm{rar}}(x), X_{\mathrm{rar}}(x'), X_{\mathrm{rar}}(0), d(x), d\left(x'\right), d(0)\right)^T \quad (44)$$

of mean vector

$$\mu = [\sigma_0,\sigma_0,\sigma_0,0,0,0] \quad (45)$$

and of covariance matrix By considering the first characteristic function we get (46) shown at the bottom of the page, and observing that $H(x,x',k_x^1,k_x^2)$ can be calculated with the derivative of its first three variables

$$\left.\frac{\partial^3\phi\left(\omega_1,\omega_2,\omega_3,\omega_4,\omega_5,\omega_6\right)}{\partial\omega_1\partial\omega_2\partial\omega_3}\right|_{0,0,0,k_1,k_2,-k_1-k_2} = j\cdot H\left(x,x',k_1^x,k_2^x\right) \quad (47)$$

we obtain (8).

APPENDIX III

The cross spectrum between the interactions of order p and q is obtained by introducing (13) in the second definition of the spectrum (see (2)). We obtain

$$S_{p,q}(k) = \gamma_{p,q}(k) + \gamma^*_{p,q}(k) \quad \text{if} \quad p\neq q \quad \text{and}$$
$$S_{p,q}(k) = \gamma_{p,q}(k) \quad \text{else} \quad (48)$$

with (49) shown at the bottom of the page. Under the Gaussian assumption of the input signal (the sea surface is assumed to be Gaussian as in [9] or [14]), $\tilde{X}(k)$ is complex, jointly Gaussian and $\tilde{X}(k_1)$ can be considered as independent of $\tilde{X}(k_2)$ if $k_1\neq\pm k_2$ [19], [21]. If one Fourier component independent of the other Fourier components is present in (49), then the mathematical expectation can be expressed as the product of the mean of this Fourier component with the mean of the product of the other Fourier components. Since $\tilde{X}(k)$ is zero mean, the expectation in (49) is null. Then, the expectation in the last part of (49) is not null only if all the Fourier components can be

$$\Sigma = \begin{pmatrix} \sigma_0^2M_2^{rr}(0) & \sigma_0^2M_2^{rr}(x-x') & \sigma_0^2M_2^{rr}(x) & \sigma_0M_2^{rd}(0) & \sigma_0M_2^{rd}(x-x') & \sigma_0M_2^{rd}(x)\\ \sigma_0^2M_2^{rr}(x'-x) & \sigma_0^2M_2^{rr}(0) & \sigma_0^2M_2^{rr}(x') & \sigma_0M_2^{rd}(x'-x) & \sigma_0M_2^{rd}(0) & \sigma_0M_2^{rd}(x')\\ \sigma_0^2M_2^{rr}(x) & \sigma_0^2M_2^{rr}(x') & \sigma_0^2M_2^{rr}(0) & \sigma_0M_2^{rd}(-x) & \sigma_0M_2^{rd}(-x') & \sigma_0M_2^{rd}(0)\\ \sigma_0M_2^{rd}(0) & \sigma_0M_2^{rd}(x'-x) & \sigma_0M_2^{rd}(-x) & M_2^{dd}(0) & M_2^{dd}(x-x') & M_2^{dd}(x)\\ \sigma_0M_2^{rd}(x-x') & \sigma_0M_2^{rd}(0) & \sigma_0M_2^{rd}(-x') & M_2^{dd}(x-x') & M_2^{dd}(0) & M_2^{dd}(x')\\ \sigma_0M_2^{rd}(x) & \sigma_0M_2^{rd}(x') & \sigma_0M_2^{rd}(0) & M_2^{dd}(x) & M_2^{dd}(x') & M_2^{dd}(0) \end{pmatrix}$$

$$\phi\left(\omega_1,\omega_2,\omega_3,\omega_4,\omega_5,\omega_6\right) = E\left\{e^{j\left(\omega_1\cdot X_{\mathrm{rar}}(x)+\omega_2\cdot X_{\mathrm{rar}}\left(x'\right)+\omega_3\cdot X_{\mathrm{rar}}(0)+\omega_4\cdot d(x)+\omega_5\cdot d\left(x'\right)+\omega_6\cdot d(0)\right)}\right\} \quad (46)$$

$$\begin{aligned}\gamma_{p,q}(k) =& E\left\{\int_{-\infty}^{+\infty}\cdots\int_{-\infty}^{+\infty} H_p\left(k-\sum_{l=1}^{p-1}k_l,k_1,\ldots,k_{p-1}\right)\tilde{X}\left(k-\sum_{l=1}^{p-1}k_l\right)\cdot\tilde{X}\left(k_1\right)\cdots\tilde{X}\left(k_{p-1}\right)dk_1\cdots dk_{p-1}\cdot\right.\\ &\left.\int_{-\infty}^{+\infty}\cdots\int_{-\infty}^{+\infty} H_q^*\left(k-\sum_{m=1}^{q-1}k'_m,k'_1,\ldots,k'_{q-1}\right)\tilde{X}^*\left(k-\sum_{m=1}^{q-1}k'_m\right)\cdot\tilde{X}^*\left(k'_1\right)\cdots\tilde{X}^*\left(k'_{q-1}\right)dk'_1\cdots dk'_{q-1}\right\}\\ =&\int_{-\infty}^{+\infty}\cdots\int_{-\infty}^{+\infty} H_p\left(k-\sum_{l=1}^{p-1}k_l,k_1,\ldots,k_{p-1}\right)H_q^*\left(k-\sum_{m=1}^{q-1}k'_m,k'_1,\ldots,k'_{q-1}\right)\\ &E\left\{\tilde{X}\left(k-\sum_{l=1}^{p-1}k_l\right)\cdot\tilde{X}\left(k_1\right)\cdots\tilde{X}\left(k_{p-1}\right)\tilde{X}^*\left(k-\sum_{m=1}^{q-1}k'_m\right)\cdot\tilde{X}^*\left(k'_1\right)\cdots\tilde{X}^*\left(k'_{q-1}\right)\right\}dk_1\cdots dk_{p-1}dk'_1\cdots dk'_{q-1}\end{aligned} \quad (49)$$

grouped by pair, the elements of this pair being complex conjugate (i.e., the wavenumber vectors are opposite). This yields to the expression given in (16) for instance. Moreover, when the number of Fourier components involved in the expectation of (49) is odd (i.e., $p + q$ is odd), this condition is never satisfied and the spectrum is always null. In the same way, the bispectrum of the Volterra model is calculated by introducing (13) in (5) and the bispectrum is non null only if $p + q + r$ is even.

REFERENCES

[1] W. Alpers, D. B. Ross, and C. L. Rulfenach, "On the detectability of ocean surface waves by real and synthetic aperture radar," *J. Geophys. Res.*, vol. 86, no. C7, pp. 6481–6498, 1981.

[2] W. Alpers and K. Hasselmann, "The two frequency microwave techniques for measuring ocean-wave spectra from an airplane or satellite," *Bound. Layer Meteor.*, vol. 13, pp. 215–230, 1978.

[3] TW Anderson, *An Introduction to Multivariate Statistical Analysis*. New York: Wiley, 1958.

[4] W. Alpers and C. L. Ruffenach, "The effects of orbital motions on synthetic aperture radar imagery of ocean waves," *IEEE Trans. Antennas Propagat.*, vol. AP-27, pp. 685–690, May 1979.

[5] C. Bruning, W. Alpers, and K. Hasselmann, "Monte-Carlo simulation studies of the nonlinear imaging of a two dimensional surface wave field by a synthetic aperture radar," *Int. J. Remote Sens.*, vol. 11, no. 10, pp. 1697–1727, 1990.

[6] M. Basseville, "Distance measures for signal processing and pattern recognition," *Signal Process.*, vol. 18, no. 4, pp. 349–369, 1989.

[7] D. Brillinger and M. Rosenblatt, *Asymptotic Theory of kth-Order Spectra (in Spectral Analysis of Time Series)*, B. Harris, Ed. New York: Wiley, 1967.

[8] D. R. Brillinger, "An introduction to polyspectra," *Annal Math. Stat.*, vol. 36, pp. 1351–1374, 1965.

[9] K. Hasselmann and S. Hasselmann, "On the nonlinear mapping of an ocean wave spectrum into a synthetic aperture radar image spectrum and its inversion," *J. Geophys. Res.*, vol. 96, no. C6, pp. 10 713–10 729, 1991.

[10] M. Hinich, "Testing for gaussianity and linearity of a stationary time series," *J. Time Series Anal*, vol. 3, no. 3, pp. 169–176, 1980.

[11] T. Hara and W. J. Plant, "Hydrodynamic modulation of short wind-wave spectra by long waves and its measurement using microwave backscatter," *J. Geophys. Res.*, vol. 99, no. C5, pp. 9767–9784, 1994.

[12] K. Hasselmann, R. K. Raney, W. J. Plant, W. Alpers, R. A. Schuman, D. R. Lyzenga, C. L. Rufenach, and M. J. Tucker, "Theory of synthetic aperture radar ocean imaging: A marsen view," *J. Geophys. Res.*, vol. 90, no. C3, pp. 4659–4686, 1985.

[13] S. B. Kim and E. J. Powers, "Orthogonalised frequency domain volterra model for non gaussian inputs," *Proc. Inst. Elect. Eng. F*, vol. 140, no. 6, pp. 402–409, 1993.

[14] H. E. Krogstad, "A simple derivation of Hasselmann's nonlinear ocean-synthetic aperture radar transform," *J. Geophys. Res.*, vol. 97, no. C2, pp. 2421–2425, 1992.

[15] H. E. Krogstad, O. Samset, and P. W. Vachon, "Generalization of the nonlinear ocean-SAR transform and a simplified SAR inversion algorithm," *Atmos. Ocean*, vol. 32, no. 1, pp. 61–82, 1994.

[16] W. C. Keller and J. W. Wright, "Microwave scattering and the straining of wind generated waves," *Radio Sci.*, vol. 10, pp. 139–147, 1975.

[17] J. M. Le Caillec and R. Garello, "Nonlinear system identification using autoregressive quadratic models," *Signal Process.*, vol. 81, no. 2, pp. 357–379, 2001.

[18] J. M. Le Caillec, R. Garello, and B. Chapron, "Two dimensional bispectral estimates from ocean SAR images," *Nonlinear Processes Geophys.*, vol. 3, pp. 196–215, 1996.

[19] J. R. Mendel, "Tutorial on higher-order statistics (spectra) in signal processing and system theory: Theoretical results and some applications," *Proc. IEEE*, vol. 79, pp. 278–304, Mar. 1991.

[20] M. Korenberg, S. A. Billings, Y. P. Liu, and P. J. McIlroy, "Orthogonal parameter estimation algorithm for nonlinear stochastic systems," *Int. J. Control*, vol. 48, pp. 193–210, 1988.

[21] C. L. Nikias and A. P. Petropulu, *Higher Order Spectra Analysis -A Nonlinear Signal Processing Framework*. Englewood Cliffs, NJ: Prentice-Hall, 1993.

[22] W. J. Plant, "A two-scale model of short wind-generated waves and scatterometry," *J. Geophys. Res.*, vol. 90, no. C9, pp. 10 735–10 749, 1986.

[23] M. Rosenblatt and J. W. Van Ness, "Estimation of the bispectrum," *Ann. Math. Stat.*, pp. 1120–1136, 1965.

[24] M. Rosenblatt, *Stationary Sequences and Random Fields*. Boston, MA: Birkhauser, 1985.

[25] A. K. Swain and S. A. Billings, "Weighted complex orthogonal estimator for identifying linear and nonlinear continuous time models from generalized frequency response functions," *Mech. Syst. . Signal Process.*, vol. 12, pp. 269–292, 1998.

[26] J. S. Schetzen, *The Volterra and Wiener Theories of Nonlinear Systems*. New York: Wiley, 1980.

[27] T. S. Rao and MM. Gabr, "A test for linearity of stationary time series analysis," *J. Time Series Anal*, vol. 1, no. 1, pp. 145–158, 1980.

[28] J. W. Wright, "Backscattering from capillary waves with application to sea clutter," *IEEE Trans. Antennas Propagat.*, vol. AP-14, pp. 749–754, May 1966.

[29] ——, "A new model for sea clutter," *IEEE Trans. Antennas Propagat.*, vol. AP-16, pp. 217–223, Mar. 1968.

Jean-Marc Le Caillec was born in Paris, France, in 1968. He received the Engineer degree in telecommunications from the École Nationale Supérieure des Télécommunications de Bretagne (ENST Bretagne), Brest, France in 1992, and the Ph.D degree in mathematics and signal processing from the University of Rennes I, Rennes, France, in 1997.

From 1997 to 1999, he was with Thomson Airsys, Paris, France, working in the area of unsupervised radar management. Since 1999, he is with ENST Bretagne, where he is now an Assistant Professor in mathematic and stochastic processes and signal processing. His main research interests are statistics, nonlinear system modeling, mathematics and signal processing for applications in remote sensing.

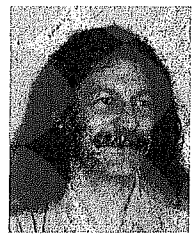

René Garello (M'85–SM'96) received the Ph.D. degree in signal processing from the Institut National Polytechnique de Grenoble (INPG) in 1981.

From 1982 to 1984, he worked as a Research Associate at the Aeronomy Lab, National Oceanic and Atmospheric Administration (NOAA), Boulder, CO. He joined the Ecole Nationale Supérieure des Télécommunications de Bretagne (ENST Bretagne), Brest, France, in 1985. Since 1988, he has been Professor in this engineering school in the field of signal processing and image processing. His main research interests lie in remote sensing, two-dimensional signal processing, and statistical and spectral analysis applied to ocean surface feature detection and characterization.

Prof. Garello started a French IEEE/OES Chapter in 1993 of which he became chairman in 1995. Since 1993 he has been involved in the organization of the Student Poster Competition for the OCEANS' series of conferences. For OCEANS'98, held in Nice, France, he was co-chair of the Technical Program Committee, Chair of the publicity Committee and Chair of the Student poster Competition. Since 1997, he has been Associate Editor for Region 8 of the IEEE JOURNAL OF OCEANIC ENGINEERING and he was elected to the OES Adcom committee in 1998. He is also an active member of the IEEE Geoscience and Remote Sensing Society.

Bertrand Chapron, photograph and biography not available at the time of publication.